BASE HEATING SENSITIVITY STUDY FOR A 4-CLUSTER ROCKET MOTOR CONFIGURATION IN SUPERSONIC FREESTREAM

Manish Mehta[1] and Francisco Canabal[1]
NASA Marshall Space Flight Center

Scott B. Tashakkor[2]
Jacobs, NASA Marshall Space Flight Center

Sheldon D. Smith[3]
Jacobs – Plumetech, NASA Marshall Space Flight Center

ABSTRACT

In support of launch vehicle base heating and pressure prediction efforts using the Loci-CHEM Navier-Stokes computational fluid dynamics solver, 35 numerical simulations of the NASA TND-1093 wind tunnel test have been modeled and analyzed. This test article is composed of four JP-4/LOX 500 lbf rocket motors exhausting into a Mach 2 – 3.5 wind tunnel at various ambient pressure conditions. These water-cooled motors are attached to a base plate of a standard missile forebody. We explore the base heating profiles for fully coupled finite-rate chemistry simulations, one-way coupled RAMP (Reacting And Multiphase Program using Method of Characteristics)-BLIMPJ (Boundary Layer Integral Matrix Program – Jet Version) derived solutions and variable and constant specific heat ratio frozen flow simulations. Variations in turbulence models, temperature boundary conditions and thermodynamic properties of the plume have been investigated at two ambient pressure conditions: 255 lb/ft^2 (simulated low altitude) and 35 lb/ft^2 (simulated high altitude). It is observed that the convective base heat flux and base temperature are most sensitive to the nozzle inner wall thermal boundary layer profile which is dependent on the wall temperature, boundary layer's specific energy and chemical reactions. Recovery shock dynamics and afterburning significantly influences convective base heating. Turbulence models and external nozzle wall thermal boundary layer profiles show less sensitivity to base heating characteristics. Base heating rates are validated for the highest fidelity solutions which show an agreement within ±10% with respect to test data.

[1] Aerospace Engineer, Aerosciences Branch (EV33), manish.mehta@nasa.gov
[2] Aerospace Engineer, Jacobs Technology, Aerosciences Branch (EV33)
[3] Aerospace Engineer, Jacobs – Plumetech, Aerosciences Branch (EV33)

1.0 Introduction

Currently, the NASA Marshall Space Flight Center Aerosciences Branch (EV33) uses semi-empirical methods derived from test data and flight data to produce launch vehicle base flow and heating environments. Flight data from the Space Shuttle, Saturn V and various wind tunnel data from the 1960s have been used. However, this methodology is only capable of enveloping the environments over broad zones, and is dependent on the limitations of the data base. This approach is also under the assumption that linear scaling can be applied to all pertinent flow parameters. This methodology cannot provide surface and volumetric distributions, deviations in base parameters or base flow physics due to launch vehicle design changes. Although the semi-empirical methodology developed by Bob Bender (retired from Qualis Corp.) et al. has provided valuable information in the past, a more physically-based approach should be implemented for the design of future launch vehicles. Accurately predicting physical mechanisms and base heating characteristics will provide design engineers with both mitigation strategies and less conservative safety factors. This may increase the payload mass, decrease the cost and improve the performance of the launch vehicle. Computational fluid dynamics (CFD) is the design tool necessary to meet these goals.

The finite-volume, fully-coupled Navier-Stokes CFD code, Loci-CHEM 3.2 (Reference 1), is being used to model and analyze base flow and heating characteristics for launch vehicles. The Aerosciences Branch has used Loci-CHEM in validating aerodynamic heating, plume impingement and plume flow field cases for ascent and stage re-entry phases (References 2 and 3). There have been limited numerical investigations and analytical formulations of base flow and base heating due to launch vehicle ascent. The main reason for these limited studies is due to the complex physics associated with multi-plume interaction base flows. Hence, the EV33 Aerothermodynamics Team has taken the task of understanding and validating these flows in detail to implement in the design and development phases of the next generation launch vehicle. This report addresses the sensitivity and physics, the comparisons between data and numerical simulations and the uncertainty analyses for base flows during launch vehicle ascent. In general, this report documents the current status of the on-going validation of the Loci-CHEM code for aerodynamic and plume-induced heating.

The engineering driver of why base heating needs to be studied is to prevent mission failure. For example, in May of 1991, the Swedish Space Corporation's Maxus sub-orbital rocket lost control and failed due to excessive base heating, burning the guidance control cables. Base heating and flow physics are important to various Branches within the Marshall Space Flight

Center (MSFC). Without an adequate thermal protection system (TPS), excessive heating may directly damage the base plate of the launch vehicle and/or various sensors and electronics that support the vehicle. The base thermal environments provided by EV33 give the Thermal Analyses and Controls Branch (EV34) with the necessary information to adequately design the TPS. The Structural and Mechanical Design Branch (EV32) can use this information to design the base and fairing regions of the launch vehicle. This report will also provide the Fluid Dynamics Branch (ER42) and the Thermal and Combustion Analysis Branch (ER43) with the sensitivity of base heating to thrust chamber conditions. By providing accurate environments around the vehicle during ascent flight, this enables various teams to install their electronics and other components in areas which will not compromise their performance. Base drag is also a large component of the total drag on the vehicle and further studied by the Aerodynamics Team in EV33.

Before addressing the numerical study, it is important to briefly discuss the general physics associated with launch vehicle ascent and base flows.

2.0 General Physics of Base Flows

As the launch vehicle ascends from the surface to space, it transitions from continuum to free-molecular flow, where the mean free path of the molecules is larger than the characteristic length (e.g. nozzle diameter). This is characterized by the Knudsen (Kn) number and is dependent on the density of the atmosphere. Most of our studies are focused within the continuum regime (Kn <1) and hence continuum mechanics formulations of fluid dynamics have been used.

Fluid flow can exist in four different regimes, (i) Stokes, (ii) laminar (iii) transition and (iv) full turbulence. Each regime shows different streamlines and flow behavior which significantly effects the aerodynamic drag, flow attachment and separation, etc. Transition from one regime to the next is dependent on the Reynolds (Re) number. Rocket plume core flows are predominantly within the fully turbulent regime due to the supersonic gas velocity. However, this does not hold true within the surface boundary layer where the flow is subsonic and laminar. This will be discussed in further detail in Section 8.0.

Launch vehicle base heating problems can be broken down into several types of flows. The following list summarizes the various categories that can occur during launch vehicle ascent.

1. Attached flow
2. Separated flow

3. Rotational flow
4. Boundary layer flow
5. Wake flows
6. Shock/shock interactions
7. Shock/boundary layer interactions
8. Multi-body viscous interactions

As can be seen, base flows lead to complex and unsteady flow fields with multiple interactions and as a result simple analytical solutions cannot be developed. However, experimental studies have provided a general insight into the physics and flow structures associated with these flows.

According to previous literature (Reference 4), there are four flow structures that directly contribute to base heating due to multiple rocket plumes: updraft plume, aspirating jet, recirculation zones (e.g. plume-induced flow separation, PIFS) and a wall jet as shown in Figure 1. These flow structures and dynamics are highly dependent on ambient pressure which is a function of the altitude in flight vehicles. The rocket plumes exhausting from multiple converging-diverging nozzles expand into the ambient atmosphere and their expansion angle is dependent on the plume expansion ratio, the ratio of the nozzle exit pressure to the ambient pressure, and the plume's specific heat ratio. This plume expansion dictates which flow structures dominate.

At low altitudes where the ambient pressure is relatively high, the plume expansion ratio is small and the overexpanded or slightly underexpanded rocket plumes do not interact with each other. This causes the free stream air to be entrained by the supersonic rocket plumes from the edge of the base and exit between the nozzles. This leads to a decrease in the base pressure and base heating with respect to the ambient atmosphere. This regime is defined as the aspirating flow regime and the entrained downward jet is known as an aspirating jet. PIFS are not observed for these types of flows.

At high altitudes where the ambient pressure is relatively low, the plume expansion ratio is large and this results in the interaction of oblique plume shock boundaries with adjacent highly underexpanded plumes. These jet shock-shock interactions result in the formation of an updraft plume within the center of the nozzle cluster. The subsonic or supersonic updraft plume impinges on the base (Figure 1) which results in maximum pressure, heat flux and temperature at the center region. Upon impingement, a wall jet propagates radially from the stagnation region as depicted in Figure 1B. This is known as a recirculating flow regime (Reference 5). At very high altitudes on the order of 110 kft, the highly expansive plumes block the freesteam air from exiting between the nozzles,

known as choked flow, and leads to maximum base heating. At these altitudes, the wall jet interacts with the freestream air which leads to the separation of the freestream air upstream of the base and this is known as PIFS.

During ascent flight, the aspirating jet transitions into a recirculating updraft plume and this is defined as the transitional flow regime (Reference 5). There is a transition point when the velocity vector is zero which leads to no convective cooling or heating. We will discuss the origin and the effects of these flow structures in more detail in Section 8.0.

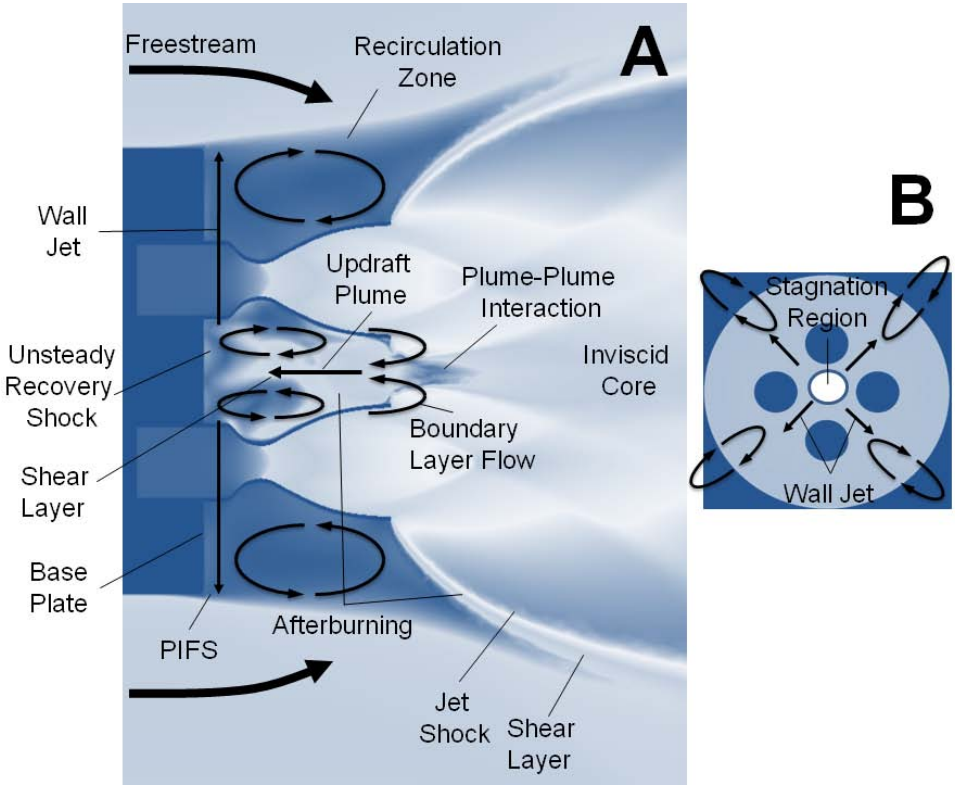

Figure 1. Fluid dynamic structures observed during complex base flows. (A) Side cross-sectional view (B) Top-down sectional view of base plate

The CFD validation process must first capture these distinct flow structures and the associated aerophysics. Once this has been satisfied, we determine if the base heat flux, temperature and pressure trends are in agreement with theory and observations. After this shows good qualitative agreement, the quantitative results are compared with test and flight data. After there is unanimous agreement with data through extensive uncertainty analyses of many numerical solutions (samples), the code can be considered validated for these flows. Hence, the methodology in determining uncertainty and validation are presented.

3.0 Uncertainty Methodology

To quantitatively determine whether a solution is validated, uncertainty analyses are required to provide support. In this case, all analyses will be done to the validation uncertainty (U_V) level. According to Coleman and Stern (Reference 6), U_V is defined by the following:

$$U_V^2 = U_D^2 + U_{SN}^2 + U_{SPD}^2 \qquad (1)$$

Where U_D is the data uncertainty, U_{SN} is the numerical solution uncertainty and U_{SPD} is uncertainty arising from using previous data. U_{SPD} is usually negligible compared to the other uncertainties. U_{SN} has two major components: the physics (e.g. boundary conditions, models) and the numerical instability. U_D has two components as well: bias and randomness. The comparison error (E) is defined as the difference between numerical simulation value (S) and the measurement value (D):

$$E = D - S \qquad (2)$$

If the comparison error is less than the validation uncertainty, the solution according to Coleman and Stern is validated to the U_V level.

$$|E| \le U_V \qquad (3)$$

Sometimes the program may define a specific tolerance to which all uncertainty needs to be satisfied and this is known as the programmatic validation tolerance or TOL_V. This implies that:

$$|E| \le U_V + TOL_V \qquad (4)$$

for a numerical solution to be considered validated by the program.

Since no bias has been documented for the various tests conducted, the U_D is assumed to be dictated by the instrument measurement uncertainty. The variance calculated by Loci-CHEM for all the state parameters are a function of both the physics and numerical instability assuming that all the boundary conditions and geometry of the problem are well matched with the test. Unfortunately, it is difficult to decouple these contributions. Hence, the total numerical solution uncertainty can be obtained by calculating the standard deviation of the solution.

4.0 Validation

The relatively well-defined wind tunnel test in Reference 7 is used for our validation efforts. Validation of CFD solutions is necessary to provide credibility to the numerical code. Without these studies, these numerical models are useless in predicting aerodynamic and aerothermodynamic environments. Since base flows are complex, EV33 is proceeding in a stepwise manner from simple to relatively complex validation cases. Also, before convergence of the conservation of energy equation is obtained, the conservation of mass and momentum need to converge to a credible solution. Hence, upon proceeding with the analyses of these flows, it is determined first if the base pressure shows good agreement with data and the general flow field characteristics are in agreement with previous observations and theory. If this does not show agreement, analysis of base heating is premature. Once convergence is obtained with mass, momentum and energy equations, the specific energy of the rocket plume at various locations within the domain are observed to see if they approach a uniform value. Once this has been achieved, full analyses of base heating and the flow fields are undertaken.

The wind tunnel test case modeled was the Musial and Ward NASA Lewis 4-cluster rocket motor configuration (Reference 7). This test case was pursued due to the well documented base heating and base pressure data for various configurations and ambient pressures. This study was well controlled and the boundary conditions were adequately documented. Other researchers have used this test case for validation of various CFD solutions such as OVERFLOW (Reference 8).

This paper methodically discusses the sensitivity study that provides insight into CFD modeling approaches to base heating problems, the aerophysics behind the various observations and the uncertainty analyses to determine validation of the numerical solutions. This paper provides an in-depth numerical investigation of base heating due to multiple-plume interactions and the best numerical modeling approaches for this problem.

5.0 Test Description

The main objectives of these tests were to provide base heating and pressure trends due to various changes in geometry configuration and ambient pressure environments. Various parameters within the geometry of the 4-cluster rocket motor configuration were studied. These rockets are attached to a base plate which is connected to a missile forebody geometry within a wind tunnel as shown in Figure 2. The geometric parameters constituted changes in nozzle area

ratio, nozzle exit angle and motor spacing and extension. The motor spacing and extension distances are normalized by the nozzle exit diameter. The motor spacing (D_s/D_e) varied from 1.67 to 2.97 and the motor extension (L/D_e) varied from 0.0425 to 1.7326. The ambient pressure within the wind tunnel was set between 12.8 lb/ft^2 and 255 lb/ft^2 to simulate various altitudes. Two converging-diverging nozzles were used: (1) a bell-shaped nozzle with an area ratio of 12, an exit half-angle of 3 degrees and an exit diameter of 2.94 inches and (2) a conical nozzle with an area ratio of 6.9, an exit half-angle of 17.5 degrees and an exit diameter of 2.2 inches. These liquid rocket engine motors used a coaxial-tube injector system with JP-4 (kerosene-based) as the fuel and liquid oxygen (LOX) as the oxidizer. A detailed description of the injector is presented in Reference 7. All rocket motors were water-cooled to reduce excessive heating to the nozzle throat walls.

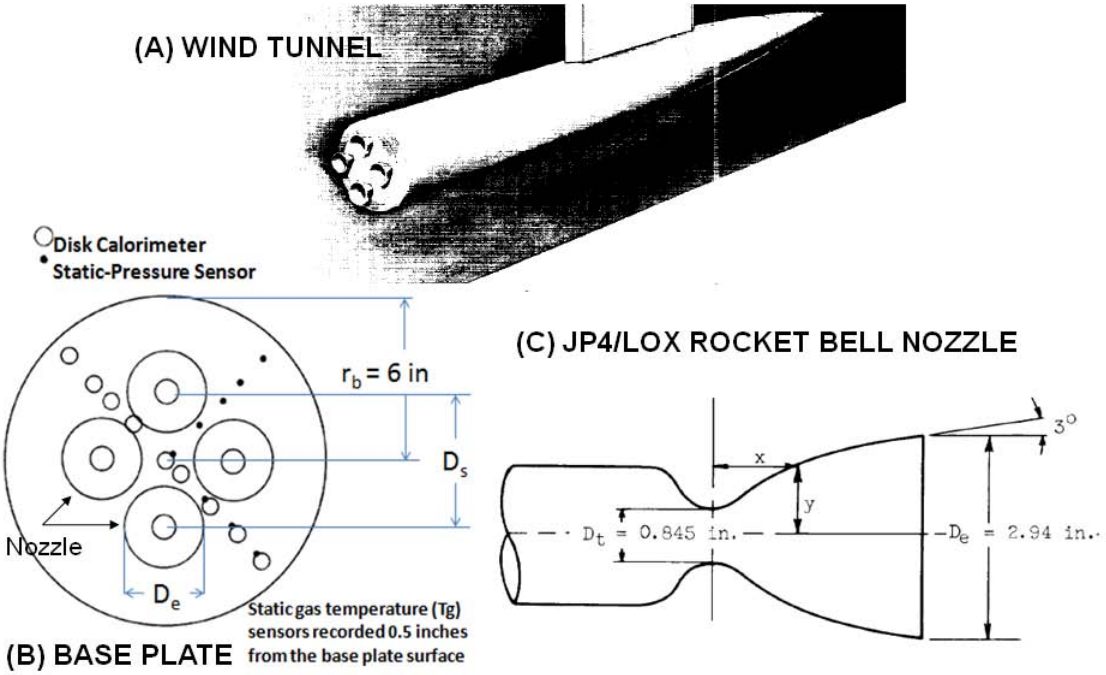

Figure 2. Schematic of NASA Lewis Supersonic Wind Tunnel Test. (A) 4-cluster rocket configuration; (B) Base plate with instrumentation; (C) Rocket nozzle bell contour

The four bell-nozzle rockets operated at steady thrust for 10 seconds in the 10 ft by 10 ft NASA Lewis supersonic wind tunnel (SWT) at a freestream Mach number between 2 and 3.5. The test report (Reference 7) concluded that the rocket motors had a nominal thrust chamber stagnation pressure and temperature of 86,400 lb/ft^2 and 5786 degrees Fahrenheit (F) and an oxidizer to

fuel ratio of 2.2. The average thrust for each rocket motor is approximately 500 pound force.

Three data products were obtained for each test: (1) base pressure, (2) base gas temperature and (3) base heat flux. Base static pressure was recorded by standard pressure transducers. The gas temperatures were measured by 0.2 inch diameter bayonet-type platinum-rhodium thermocouples which extended ½ inch above the base plate and were sampled at 100 Hz. The total heat flux was measured by 0.375 inch diameter copper disk calorimeters and recorded at 0.75 Hz frequency at a constant base plate wall temperature of 150 deg F. Each data point recorded in Reference 7 is obtained by recording only the maximum value at that location during the 10 second duration. The location of each pressure transducer, thermocouple and calorimeter on the base plate are shown in Figure 2. The uncertainties due to the pressure transducer, thermocouple and calorimeter are 2%, 0.1% and 5% of the full-scale value, respectively (Reference 17-19). Due to many experimental tests presented in Reference 7, the numerical study focuses on two specific cases described below.

6.0 Numerical Methodology

To most accurately simulate rocket nozzles employed on future launch vehicles, the bell nozzle configuration was chosen to be modeled. Also, the modeled test configuration had a nozzle extension (L) of 1.53 D_e and nozzle spacing (D_s) of 1.67 D_e. The numerical study focused on two different ambient pressure conditions: 35 lb/ft^2 and 255 lb/ft^2. According to atmospheric tables, this correlates to a simulated altitude of 91 kft (high altitude case) and 49 kft (low altitude case), respectively. Although freestream Mach number was experimentally observed to be insensitive to base heating, the wind tunnel numerical domain was set to Mach 2.75. The specific conditions are recorded in Table 1.

Table 1. Modeling boundary and initial conditions

Parameters	**Simulated High Altitude**	**Simulated Low Altitude**
P_∞ - ambient (lb/ft^2)	35	255
T_∞ (F)	76.4	76.4
M_∞	2.75	2.75
Simulated Altitude (ft)	90,700	48,900
P_c – thrust chamber (lb/ft^2)	86,400	86,400

T_c (F)	5786	5786
Re	5×10^6	5×10^6
Jet expansion ratio	24.7	3.4

This study resulted in the design and development of five different geometries and grids and the modeling of 35 different numerical simulations. The 3-D geometry was designed and developed by using line drawings, specifications and linear scaling of some components, as shown from Figure 3, that did not have associated dimensions. The sting was not included in the numerical model, because it was located significantly up-stream of the base region (~10 D_e). As a result, its effects were considered negligible. The geometry and surface mesh were modeled using Solidmesh 5.7.2 (Reference 9). Various sharp corners within the geometry were slightly rounded so that the flow structures in their vicinity could be numerically resolved. The base region and inner nozzle domain had the highest grid resolution to adequately resolve all the flow structures and boundary layers within this region. The unstructured volume and boundary layer grids were populated by Advancing-Front/Local-Reconnection (AFLR3) 12.9.10 unstructured grid generator (Reference 10). Grid convergence was also achieved by comparing the 20 million and 30 million cell meshes. Within this study, only the 30 million cell grid was used for analyses.

The boundary conditions implemented on these numerical models are schematically shown in Figure 3. The wind tunnel surrounding walls were modeled as far-field conditions due to minimal wall interference effects and the inlet and exit of the wind tunnel were set to inflow and outflow conditions. The calculated blockage ratio for these tests is 0.8%. According to Burley and Harrington (Reference 25), a blockage ratio less than 1% will present minimal changes in the pressure and flow field distributions due to wall interference. All wall surfaces were modeled as no-slip viscous walls with varying wall temperature conditions based on the test report. Isentropic inflow boundary condition was implemented at the thrust chamber inlets. It is important to note that the entire nozzle inner wall (Iwall) temperature was varied from the adiabatic conditions to as low as 440 deg F. From analytical calculations, the Iwall temperature was determined to be approximately 800 deg F due to the removal of some of the combustion heat to the surrounding water-cooled heat exchangers. This is also confirmed by literature with similar initial conditions (Reference 21). The external wall temperatures of the base plate and nozzles (Twall) were set at 150 deg F as noted experimentally. No symmetry planes were used, because this will artificially force a symmetric solution despite the fact that

these flows are highly unsteady. In general, we varied the wall temperature conditions and the thermodynamic, chemistry and turbulence models.

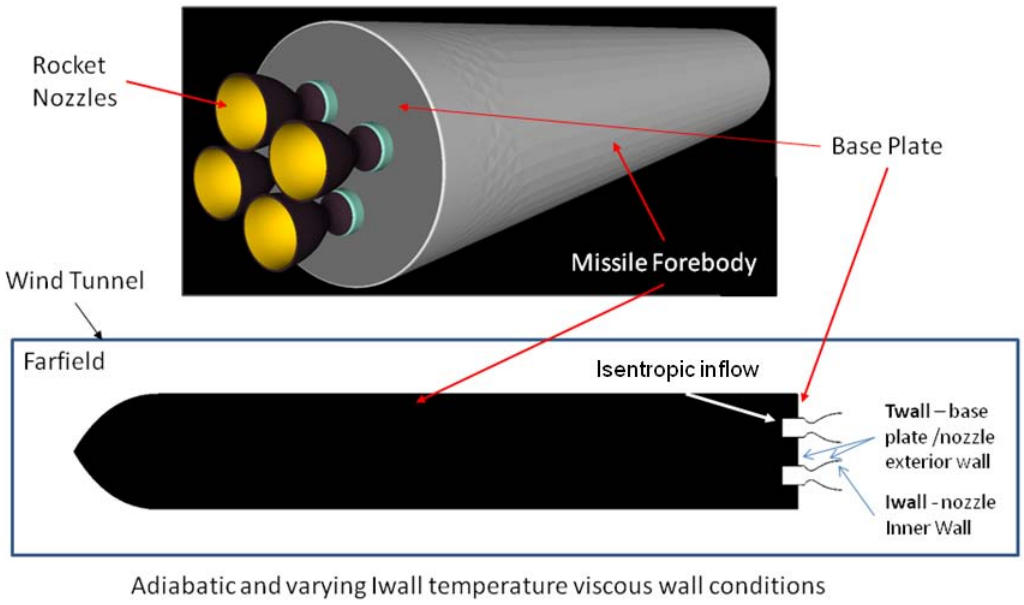

Figure 3. 3-D geometry and locations of various boundary conditions

The thermodynamic models that are compared in this study are presented from smallest to highest degree of fidelity (Table 2): (1) constant Cp/Cv (equivalent species/frozen flow); (2) variable Cp/Cv (equivalent species/frozen flow) and (3) finite-rate chemistry. Cp is the plume specific heat at constant pressure and Cv is the specific heat at constant volume. Equivalent species/ frozen flow (no modeling of chemical reactions) solutions model the individual exhaust plume gases obtained from the NASA Lewis Chemical Equilibrium Composition (CEC) Library (Reference 14) as one averaged equivalent gas and does not account for chemical reactions. The fidelity of the thermodynamic model is increased by implementing a variable plume specific heat ratio into Loci-CHEM. The variable Cp/Cv is a function of static temperature which is derived empirically. The modeling of finite-rate chemistry into the full Navier-Stokes equations is more complex as it requires more computational resources in solving an extra conservation of mass equation for each species. The chemistry model used in the simulations was a 10 species RP-1/liquid oxygen (LOX) model (Reference 11). The specific heat ratio for each exhaust plume species is modeled as an empirical function of the temperature (similar to the variable Cp/Cv thermodynamic model).

These chemical interactions were not modeled from the injectors, but rather further downstream of the thrust chamber where residual fuel and oxidizer

react. JP-4 fuel database is not included in Loci-CHEM and as a result, a very close cousin of this fuel, the RP-1 has been used for modeling. Both fuels have a high concentration of kerosene. These thermodynamic models have been used in the past for launch vehicle designs by EV33, but a detailed sensitivity study has not been performed on these models. This chemistry model has been implemented for the first time in the Loci-CHEM code for base heating applications.

Menter's Baseline (BSL) Model and Menter's Shear Stress Transport (SST) Model are used for comparing turbulence model sensitivity. For all of our cases, the BSL model has been incorporated. These Reynolds-Averaging Navier-Stokes (RANS) turbulence models are unique in that they solve the classic Wilcox *k* - ω turbulence model within the wall region and switch to *k* (turbulent kinetic energy) - ε (turbulent kinetic energy dissipation) model away from the wall (Reference 12). This is implemented to prevent the high turbulent eddy-viscosity sensitivity within the boundary layer to the freestream vorticity (ω) as observed in the Wilcox *k* - ω model. BSL is used for predicting free shear flows and the SST is mainly used for predicting adverse pressure gradient flows. SST also produces relatively larger turbulence levels in regions with normal shear strains such as stagnation regions and regions of strong accelerations. Hence, all simulations were modeled with BSL.

The numerical simulation analyses only accounts for convective heating and does not take into consideration radiative heating or high temperature particle impacts. The calorimeters record the total heat flux which is a function of both convective and radiative heating rates and defined by Equation 5a.

$$\frac{\dot{q}}{A_w} = \left(\rho c_p d\right)_{disk} \frac{dT}{dt} = h\left(T_r - T_w\right) + \sigma\varepsilon\left(T_p{}^4 - T_w{}^4\right) \qquad (5a)$$

Total Heat Flux = Convection + Radiation

Where q is the total heat flux per unit area, T_r is the recovery temperature, T_w is the base plate wall temperature, T_p is the plume gas temperature, h is the convective heat transfer coefficient, σ is the Stefan-Boltzmann constant, ε is the emissivity of the calorimeter, c_p is the specific heat capacity of the calorimeter, A_w is the area of the base plate, d is the diameter of the calorimeter and ρ is the density of the calorimeter material. Unfortunately, radiometers or spectrometers were not placed at the base plate and hence no radiative heat flux has been recorded.

However, convective heating is the main driver and radiative heating plays a minor role for this test case. The reason for this is many-fold. Assuming soot

(ε_s) and plume gas (ε_p) has an emissivity of 0.8 and the aluminum oxide coated base plate (ε_w) has an emissivity of 0.41 (Reference 23) and substituting plume gas and base plate temperatures, T_p and $T_{w,}$ in Equation 5b, a simple analytical calculation shows that the maximum radiative heat flux possible for our test cases are on the order of 5 BTU/ft^2-s, approximately 5-10% of the total heat flux recorded experimentally. It should be noted that the surface area of the plume, A_p, is calculated assuming a ½ a spheroid. $F_{1\text{-}2}$, the view factor, is assumed to be one where all the radiation from the plume intersects the base plate. Equation 5b takes into account the radiation imparted to the base plate by both the soot and plume gas components (Reference 24).

$$\frac{\dot{q}}{A_w} = \frac{\sigma\left(T_p{}^4 - T_w{}^4\right)}{\frac{1-\varepsilon_p}{A_p\varepsilon_p} + \frac{1}{A_p F_{1-2}} + \frac{1-\varepsilon_w}{A_w\varepsilon_w}} + \frac{\sigma\left(T_p{}^4 - T_w{}^4\right)}{\frac{1-\varepsilon_s}{A_p\varepsilon_s} + \frac{1}{A_p F_{1-2}} + \frac{1-\varepsilon_w}{A_w\varepsilon_w}} - \frac{\sigma\left(T_p{}^4 - T_w{}^4\right)}{\frac{1-\varepsilon_s\varepsilon_p}{A_p\varepsilon_s\varepsilon_p} + \frac{1}{A_p F_{1-2}} + \frac{1-\varepsilon_w}{A_w\varepsilon_w}} \tag{5b}$$

Radiation becomes considerably important when solid particles are introduced within the exhaust plume. This is an important consideration when working with solid rocket motors in which solid particles contribute 15% to 30% of the mass flow (Reference 22). Solid particles mainly in the form of aluminum oxide can increase the radiative heat flux by a factor of 2 to 10. Solid particles also raise the plume temperature considerably, increasing both the convective and radiative flux components. Since the test case is a JP-4/LOX liquid rocket engine, solid particles are relatively negligible and the main solid particle component is soot which makes approximately 1-2% of the mass flow. The radiation is also a function of plume geometry and since this is a small scale test model, the plume diameters are considerably smaller by a factor of 20 as compared to the full-scale flight vehicles. Radiation which is also a function of ambient pressure and temperature is more important during the first 20 kft of flight. These simulations were done at simulated altitudes greater than 40 kft. As a result, the assumption that the heating rates are governed by convection is valid for this test case.

The full Navier-Stokes conservation of mass, momentum and energy equations were implicitly solved at a maximum pseudo time step size of 1 x 10^{-3} seconds. All simulations described in the paper were modeled at steady-state flow conditions using a second-order inviscid flux limiter, second order in space and implicit Euler temporal integration, Wilcox compressibility correction, Sutherland's Law to calculate various plume transport properties and the diffusion model was governed by a constant Schmidt number of 0.9 within the laminar region. It should be noted that the diffusion and transport models within the turbulent regime are dictated by the turbulent eddy viscosity calculated by the

turbulence conservation equations. For the nozzle internal flow solutions (shown in Figure 14), the higher fidelity CHEMKIN transport library was used. The mean, variance and covariance of the important parameters were solved for sample sizes greater than 6000 iterations.

Convergence of the solution was determined by inspecting the convergence of three profiles: (1) the residuals for conservation of mass, momentum and energy; (2) various probes within the numerical domain such as at the nozzle exit and base plate region; and (3) average energy flux on the base plate. Once all of these profiles were steady, the base pressure, temperature and heat flux solutions were extracted and imported into a post-processing MATLAB code. This code provides automated data-simulation comparison and uncertainty line plots for analyses.

7.0 Results

In order to understand the sensitivity and physics of base heating due to multiple plume interactions, we developed a sensitivity study which systematically varies the nozzle inner wall (Iwall) and nozzle external wall and base plate (Twall) temperatures, and the thermodynamic, chemistry and turbulence models. Table 2 provides further details to the sensitivity study. The Twall values were changed from 0 deg F to 150 deg F, but this lead to negligible changes in state profiles. Base heating trends and characteristics showed little difference (<2%) between Menter's baseline turbulence (BSL) model and the shear stress (SST) transport turbulence model. The imposed boundary conditions and thermodynamic and turbulence models used in this study have customarily been used by EV33.

However, two novel modeling approaches were used: (1) the numerical domain of the nozzle interior up to the thruster chamber was solved by the fully-coupled Loci-CHEM solver and (2) RP-1/LOX chemistry model was implemented for base heating applications. EV33 customarily solves the nozzle internal flow solution with RAMP2-BLIMPJ, Reacting And Multiphase Program using Method of Characteristics - Boundary Layer Integral Matrix Program – Jet Version (Reference 13), and this solution provides a prescribed boundary condition that is imposed somewhere in the diverging section of the nozzle. Loci-CHEM uses this prescribed boundary condition to solve the full numerical domain for determining base heating calculations. The numerical models mentioned above have been used by the Branch, but a detailed sensitivity study of these models has not been performed for base heating applications. *Hence, these efforts are to provide the Branch with the most accurate modeling approach in solving complex base heating problems.*

Table 2. Varying modeling parameters for sensitivity study

Test Cases	Twall (F)	Iwall (F)	Comments
Variable Cp/Cv	150	800	Equivalent plume species with varying c_p as a function of temperature. c_p (T) is empirically derived by the NASA Lewis CEC Library (Reference 14). Defined as frozen flow.
Cp/Cv = 1.15	150	800	Equivalent plume species with constant c_p determined at the thrust chamber section from the NASA Lewis CEC.
Finite-rate chemistry	150	800	10 major plume species are modeled with empirically derived c_p(T) and 17 major chemical reactions for RP-1/LOX are modeled with empirically derived reaction rates calculated from the Arrhenius eqn.
Iwall=adia, Variable Cp/Cv	150	Adiabatic	Similar thermodynamic model as Variable Cp/Cv. Nozzle inner wall (Iwall) is adiabatic.
Iwall=adia, Cp/Cv=1.15	150	Adiabatic	Similar thermodynamic model as Cp/Cv =1.15. Nozzle inner wall (Iwall) is adiabatic.
Test Data	150	Unknown	

We show comparison line plots of the static pressure (Figure 4), gas temperature (Figure 5) and heat flux (Figure 6) at the base plate between the numerical solutions and the test data which are observed at two different ambient pressure conditions. This shows a general comparison between the base flow trends at two different simulated altitudes. The gas temperature (Tg) is normalized with respect to the thruster chamber stagnation temperature (Tc). The radial distance along the base plate (r) is normalized with respect to the base plate radius (r_b) as depicted in Figure 2.

The base distribution of temperature, pressure and heat flux show similar gross trends between numerical simulations and experimental data. There is a maximum peak in these parameters at $r/r_b = 0$ for all cases. This peak is much larger for the simulated high altitude cases as compared to low altitude. All surface mean distributions are symmetric. However, these parametric distributions are asymmetric for instantaneous converged solutions. According to Figure 4, the simulated low altitude case shows a decrease in surface pressure of 100 lb/ft^2 as compared to the high altitude case. The surface heat flux of the high altitude case is greater by 100% as compared to the low altitude case (Figure 6).

As observed in Figures 5 and 6, the base gas temperature and heat flux were the highest in magnitude for the cases where the Iwall is adiabatic (shown in dashed lines) with the plume at a constant specific heat ratio. These distributions were the lowest in magnitude for the cases where the Iwall temperature is at a constant 800 deg F (shown as solid lines) with the plume at a

variable specific heat ratio. The base pressure distributions did not change significantly between the various cases.

The main objective of this study is to observe how changing the Iwall temperature, chemistry and plume thermodynamic properties affect base heating parameters and to determine how they compare to test data. This has two functions: (1) it provides the sensitivity of the numerical code and (2) provides insight into the physics of base heating. The first component is addressed in this section. Figures 4-6. show that implementing finite-rate chemistry into the numerical code and accurate modeling of the Iwall temperature results in the best agreement of numerical results with the test data. This is observed for all parameters within the base region: static pressure, gas temperature and heat flux. As the thermodynamic properties of the exhaust plume are simplified, such as variable and constant specific heat ratio, and frozen flow conditions, a larger deviation from the test data is observed in both the base heat flux and base temperature.

The rocket motors are water-cooled and hence the assumption of an adiabatic nozzle inner wall is incorrect. The combustion heat is absorbed by the cool Iwall and transferred to the circulating water in tubes surrounding the motors. This reduced the wall temperature and the regenerative cooling mechanism prevents the melting of the nozzle throat and structure failure. Since these boundary conditions were not specified in the report, the Iwall temperature was varied from 440 deg F to 2500 deg F as indicated by Reference 21 to be a feasible range. According to 1-D heat transfer analyses done with the recorded thruster stagnation temperature and water-cool system, 800 deg F was determined to be the most accurate Iwall boundary condition. A much better agreement with data is observed when an accurate Iwall boundary condition is modeled.

From qualitative observation, a cool Iwall boundary condition with finite-rate chemistry modeling shows the best agreement with data. However, there is a decrease by 15% of this numerical solution as compared to data for base pressure calculations at low altitude (Figure 4). Since the base perimeter values are also low by this value, this could be an effect due to small changes within the ambient pressure surrounding the base region. Depending on the strength and angle of the shockwaves propagating from the missile nose cone down to the base region, which is a function of the missile length and diameter, the ambient static pressure can change. Unfortunately, these parameters were not documented in the report and may have lead to the minor deviation. However, the main driver behind this decrease in base static pressure is believed to be associated with Loci-CHEM's over-prediction of freestream entrainment in this region. This will be discussed further in the following Section.

Another discrepancy is the deviation of the nondimensional gas temperature distribution for the simulated high altitude case (Figure 5). The regenerative cooling mechanism and radiation losses reduce the base gas temperature and consequently result in a lower nondimensional ratio. Unfortunately, the exterior nozzle wall temperature profiles were not recorded in the experiment. Due to a smaller number density of freestream molecules at the simulated high altitude case, the sensitivity to changing pressure and temperature are more pronounced than at the low altitude case. In other words, the high number density freestream condition "dampens" both the pressure and temperature response to either the updraft plume or other perturbations.

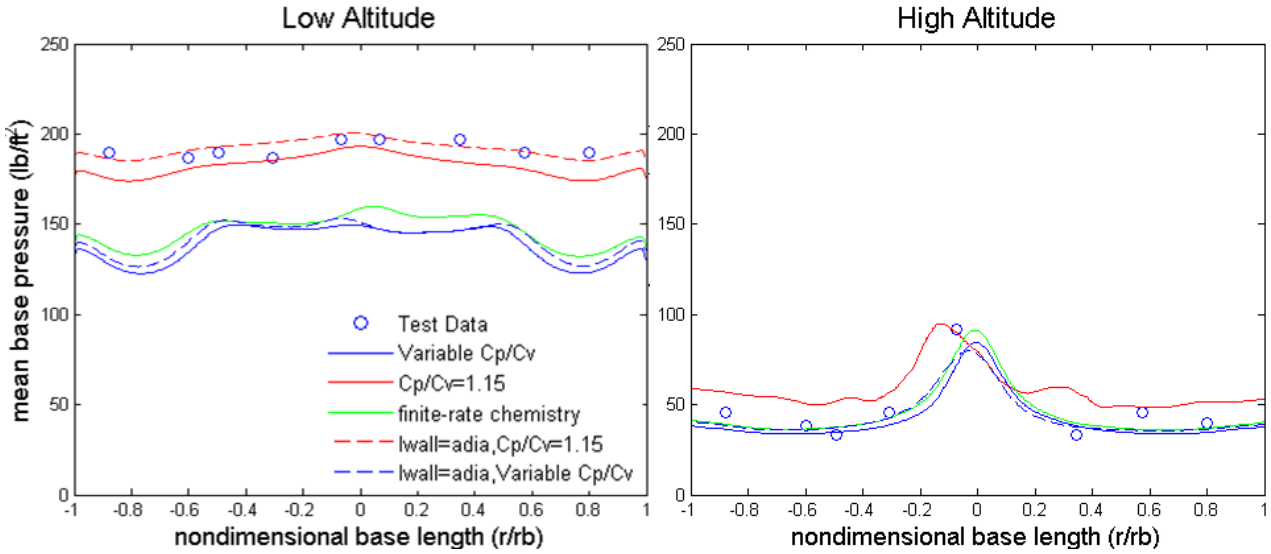

Figure 4. Mean base pressure profiles at simulated low (left) and high (right) altitudes. Solid lines correlate to an inner nozzle wall (Iwall) temperature of 800 deg F and the dashed lines correlate to an adiabatic inner nozzle wall

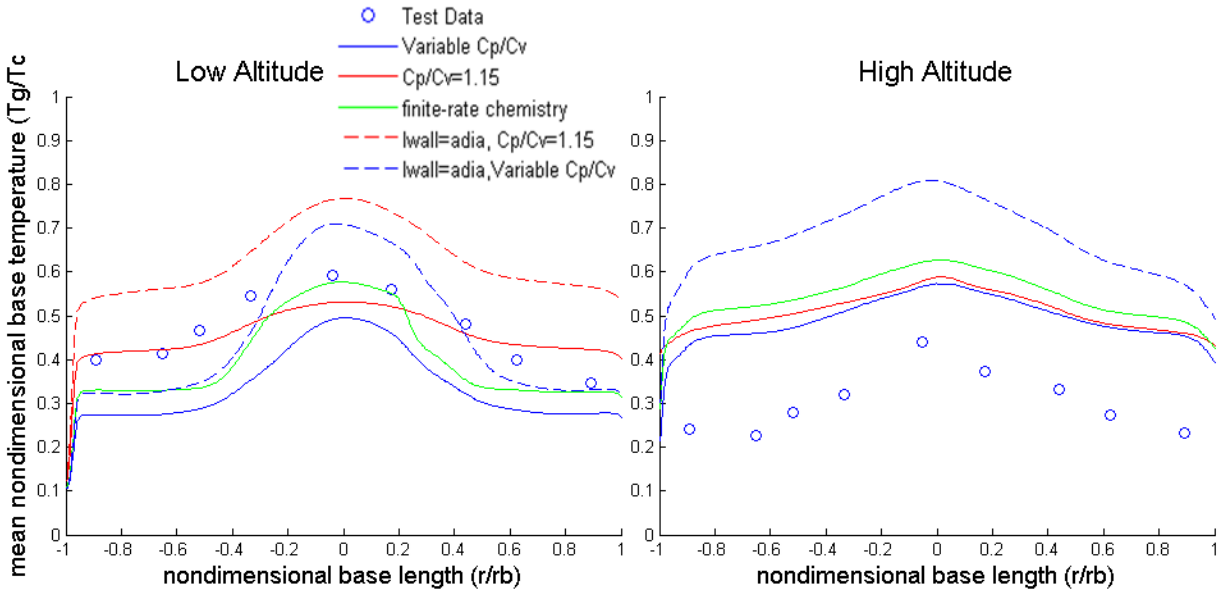

Figure 5. Mean nondimensional base gas temperature profiles at simulated low (left) and high (right) altitudes. Solid lines correlate to an inner nozzle wall temperature of 800 deg F and the dashed lines correlate to an adiabatic inner nozzle wall.

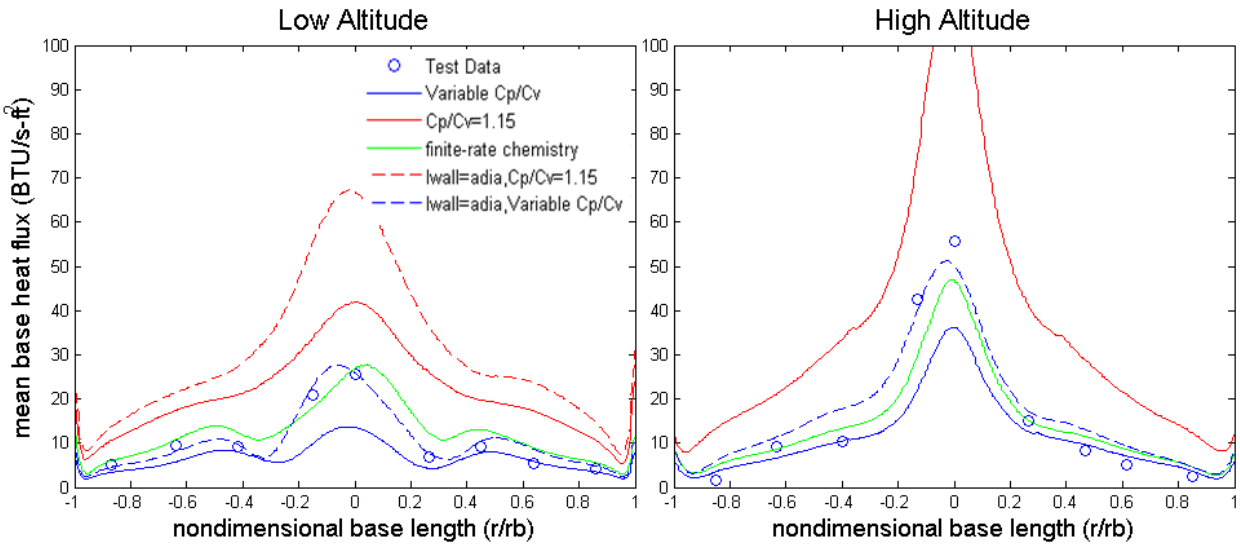

Figure 6. Mean base heat flux profiles at simulated low (left) and high (right) altitudes. Solid lines correlate to an inner nozzle wall temperature of 800 deg F and the dashed lines correlate to an adiabatic inner nozzle wall.

8.0 Aerophysics

This section will first describe the general physics associated with base flows. Then the sensitivity of the Iwall thermal boundary layer will be discussed and its effect on base heating. Finally, this section will discuss other major physical mechanisms that influence base heating.

8.1 Flow Field

Each of the rocket exhaust plumes at simulated high and low altitudes are underexpanded jets. At simulated low altitude, the jet shock is attenuated by the interaction and mixing of the shock with the dense shear layer at the jet boundary which may lead to Kelvin-Helmholtz instabilities. The higher ambient pressure results in larger shear forces and pinches the jet sooner, leading to an axial increase in the turbulent mixing layer (Figure 7). Hence, the decay of the supersonic core is observed. It can be seen that for the high altitude case, the supersonic core is well preserved with little attenuation. All contour plots, unless specified, are sectional planes through the centerline of two nozzles.

There is also a difference in the updraft plume structure between high and low altitudes. It can be seen from Figure 7 that a well-developed supersonic plume is developed for the high altitude cases and a subsonic plume for the low altitude case. The origin and its effects will be discussed in more detail in Section 8.3.

Due to the different nature of the updraft plumes for the two cases, the base heat flux contours are significantly different as well as shown in Figure 7. However, the mean flux distributions for both cases show symmetry as observed in experimental data. Since the framework for macroscale aerophysics has been addressed, the investigation at the microscale level is presented below.

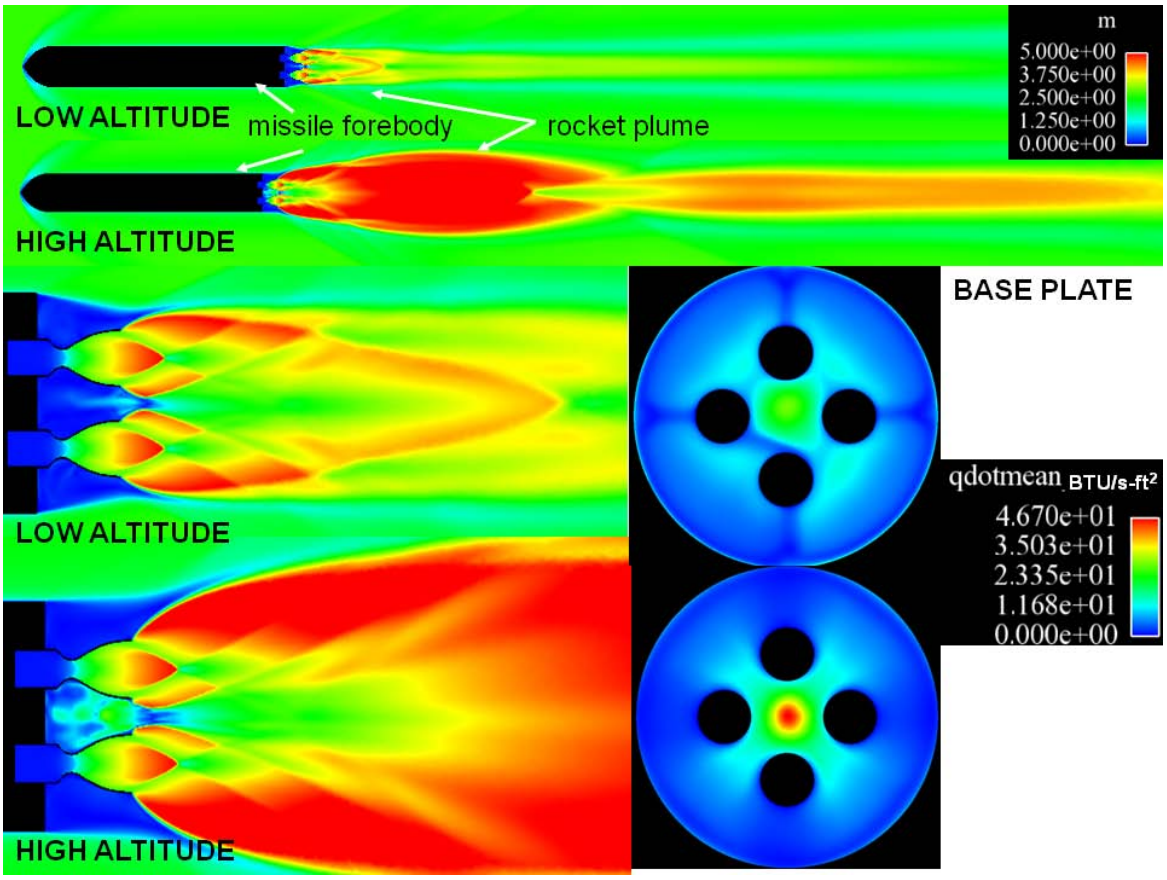

Figure 7. (Top) Full wind tunnel flow field domain (Mach contour); (Bottom left) Base flow field domain (Mach contour); (Bottom right) Base heat flux contours

8.2 Thermal Boundary Layer

8.2.1 Nozzle inner wall (Iwall) temperature

As noted earlier, the Iwall temperature boundary condition between 800 deg F and adiabatic leads to considerable differences in both the base heat flux and gas temperature profiles. These large deviations originate from differences in the Iwall thermal boundary layer. Leaving all other parameters the same for each model, the Iwall temperature conditions were varied between 440 deg F and adiabatic wall. The x-axis in Figure 8 is the nondimensional slice near the nozzle exit (normalized by the nozzle exit diameter, D_e) and the y-axis is the nondimensional static temperature (normalized by the chamber stagnation temperature, Tc). To be more precise, all sectional slices near the nozzle exit are at x = 2.8213 in where x = 0 in is at the nozzle throat. The axis at $x/D_e = 0$ is at

the wall. This profile is taken to show both the boundary layer and freestream regions.

Adiabatic wall assumes no heat transfer losses to the wall and as a result the wall temperature approaches the recovery temperature (Tg/Tc ~0.9) and this leads to a higher thermal energy component within the boundary and considerable changes in the thermal boundary layer profile. All profiles are modeled with variable Cp/Cv thermodynamics. It can be seen that there is a +20% increase (Figure 8) in the areal-thermal boundary layer profile between the Iwall 800 deg F (solid blue curve) and adiabatic wall boundary conditions (dashed blue curve) which leads to an average increase of 70% in the base center heat flux (Figure 6) and ~45% in the base center gas temperature (Figure 5). It can also be seen that the (dT/dy) slope for the two Iwall boundary conditions within the boundary layer are opposite in signs which leads to different heat transfer flow directions (toward or away from the nozzle wall). All profiles for the various Iwall conditions converge within the freestream region.

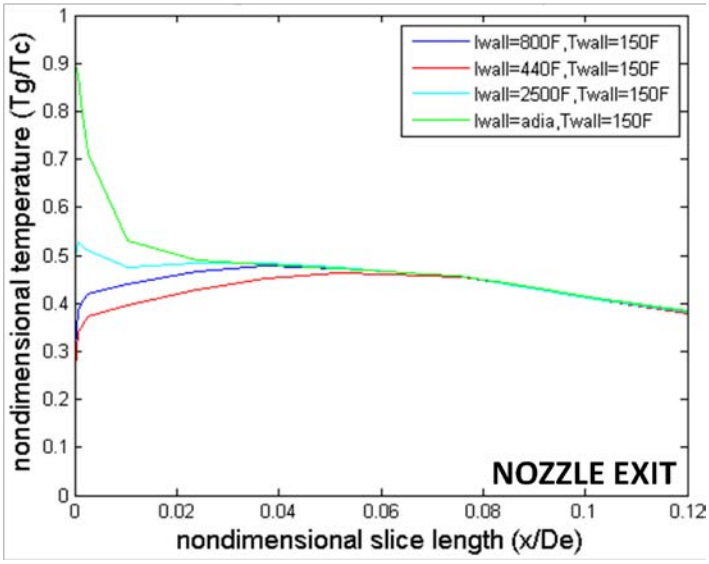

Figure 8. Nondimensional temperature vs. nondimensional slice length near the nozzle exit for changing Iwall temperature with the variable Cp/Cv thermodynamic model

8.2.2. Specific energy and thermodynamic models

Besides the Iwall temperature effect on the thermal boundary layer, the thermodynamic and chemistry models have a large effect on the profiles as observed in Figure 9. Figure 9 is a plot of the nondimensional temperature as a function of the nondimensional exit slice length for three models: (1) variable

Cp/Cv frozen flow; (2) constant Cp/Cv frozen flow and (3) variable Cp/Cv finite-rate chemistry. These differences are larger than those imposed by varying the Iwall temperature boundary conditions. These differences are attributed in their approach to modeling the plume molecules specific energy.

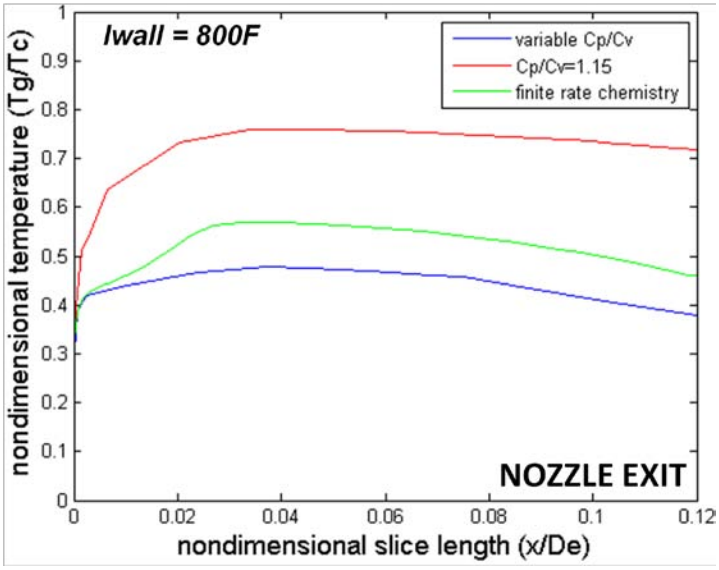

Figure 9. Nondimensional temperature vs. nondimensional slice length near the nozzle exit for varying thermodynamic and chemistry models at an Iwall temperature of 800 deg F.

The plume's specific internal energy (e_T) is broken down into four forms of energy as shown in Equations 6-8: (1) translational (e_{tr}); (2) rotational (e_{rot}); (3) vibrational (e_{vib}) and (4) electronic (e_{elect}) (Reference 15). This holds true for diatomic gas molecules, but for monatomic molecules there is only the translational energy component. They each become activated at different temperatures.

$$e_T = e_{tr} + e_{rot} + e_{vib} + e_{elect} \qquad (6)$$

$$e_T = \frac{3}{2}RT + RT + \frac{R\theta_v}{e^{\theta_v/T} - 1} + e_{elect} \qquad (7)$$

$$\theta_v = \frac{h\nu}{k} \qquad (8)$$

Where Θ_v is the characteristic temperature for vibration, h is the Planck constant, v is the harmonic frequency, k is the Boltzmann constant and R is the gas constant. The $e_{elec\mathrm{t}}$ term is considered negligible due to the narrow range of practical temperatures used in our study. To apply this directly to specific heat ratio (γ), Equation 7 becomes:

$$\frac{h_T}{e_T} = \frac{e_T + RT}{e_T} = \frac{c_p}{c_v} = \gamma \qquad (9)$$

h_T is the molecular total specific enthalpy. Substituting Equation 7 into Equation 9, the specific heat ratio becomes:

$$\gamma = \left[1 + \frac{1}{\frac{5}{2} + \frac{\theta_v}{T\left(e^{\theta_v / T} - 1\right)}} \right] \qquad (10)$$

Figure 10 shows the profiles of the variable and constant specific heat ratio as a function of temperature implemented into our models. It can be seen from Equation 10 that the drop in gamma is due to the gas molecules entering the vibrational energy regime. This brings us to how each of the three thermodynamic models shown in Figure 9 leads to different thermal boundary layer profiles. From classical kinetic theory, temperature is a function of the gas molecules translational specific energy. Constant Cp/Cv case only accounts for translational and rotational energies at a specific location within the nozzle, whereas the variable Cp/Cv also takes into consideration the vibrational energy term. As a result, when the specific energy of the plume molecules increase due to a rise in temperature above the vibrational characteristic temperature for the constant Cp/Cv model, the excess energy is not allocated to the vibrational mode but rather to the rotational and translational modes. This artificially leads to higher plume temperatures as observed in the thermal boundary layer profile. The variable Cp/Cv model moves the excess specific energy into vibrationally exciting the plume molecules and results in a decrease in the plume temperature and boundary layer thermal energy. As a result, base heat flux values are considerably different between these two models (Figure 6).

The finite-rate chemistry also accounts for chemical reactions within the boundary layer which may lead to the formation and destruction of various species and as a result the species-averaged specific heat ratio – temperature distribution may be considerably different than what is presented in Figure 10. As

a result, the rise in temperature within the nozzle boundary layer as compared to the variable Cp/Cv model in Figure 9 is due to the release of chemical energy with the recombination of plume species. These differences are not only observed within the boundary layer, but also extend to within the freestream region. The finite-rate chemistry solution (solid green curve) shows an increase of 20% in the areal-thermal boundary layer profile (Figure 9) as compared to frozen flow solution (solid blue curve) and this causes an average increase of 60% in the base heat flux and 20% in the gas temperature within the base center region (Figure 6).

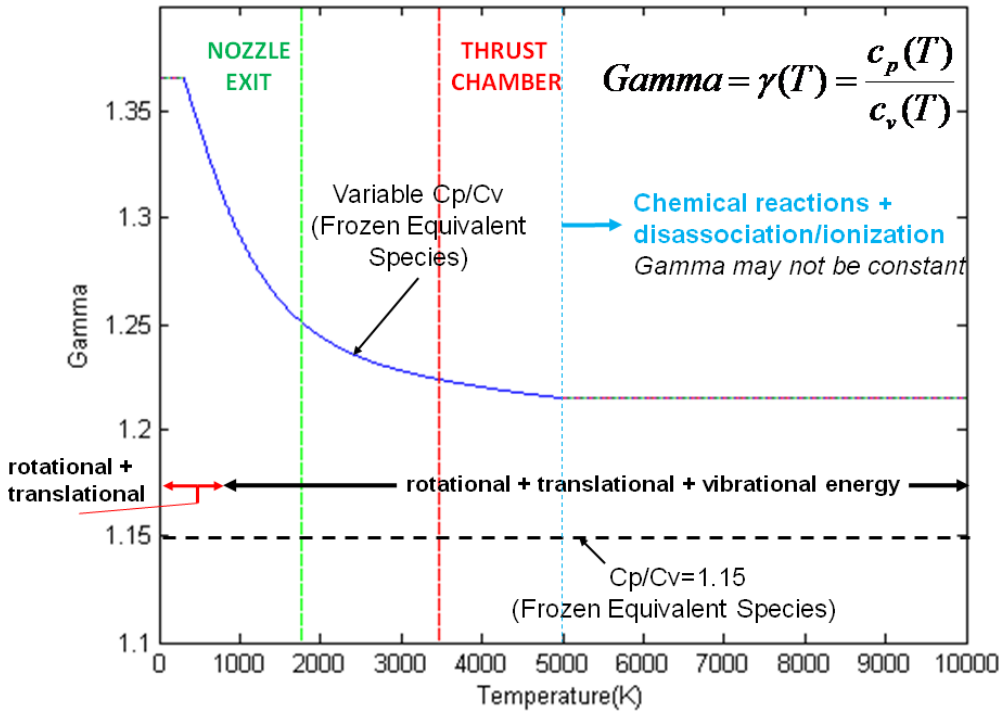

Figure 10. Specific heat ratio as a function of temperature for equivalent plume species – frozen flow

8.2.3 RAMP2-BLIMPJ and Loci-CHEM modeling comparisons

We present the base heating characteristics imposed by two different modeling approaches. As briefly described earlier, the main modeling approach implemented by EV33 for base heating investigations is to use the one-way coupled RAMP2-BLIMPJ 2-D Method of Characteristics (MOC) code (Reference 13) to generate the internal flow solutions with finite-rate chemistry and then to generate a prescribed boundary condition at the nozzle diverging section. The fully-coupled Navier-Stokes Loci-CHEM solver uses this prescribed boundary condition to model the full numerical domain. The RAMP2-BLIMPJ methodology leads to some minor concerns in using a one-way coupled MOC nozzle flow

solution where MOC provides initial conditions to the boundary layer equations. This also leads to some concerns on whether the thermal boundary layer thickness and profiles would be consistent between the two codes. Figure 11A and B show the static temperature contours within the base region between the two approaches. As observed in Figure 11C where x/D_e = 0.99 at the nozzle wall, it can be seen that there is only a deviation of less than 3% within the thermal boundary layer. This leads to minor deviations within the base heat flux and base gas temperature distributions between the two codes as shown in Figure 11D. The Mach Disc locations are identical for the two approaches. These deviations are on the order of the validation uncertainty and therefore it is difficult to ascertain which approach is more accurate. However from the comparison error calculation (Equation 2), the Loci-CHEM nozzle interior flow solution approach shows a better agreement with test data. This again proves that the thermal boundary layer profile has a large effect on base heating characteristics.

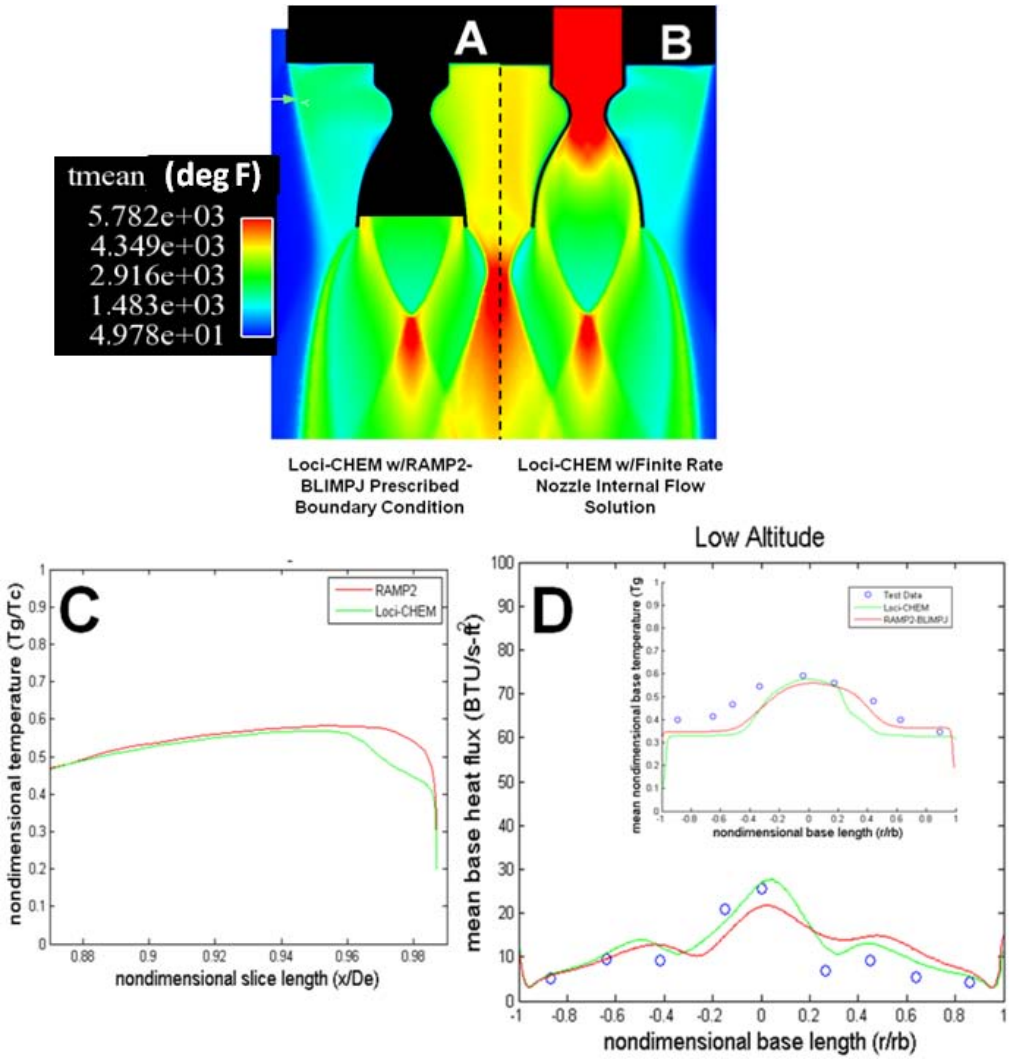

Figure 11. Comparison of mean static temperature contours between the (A) RAMP2 modeling approach and the (B) Loci-CHEM nozzle internal flow solution modeling approach at simulated low altitude; (C) Thermal boundary layer profile comparison between Loci-CHEM and RAMP2 modeling approaches; (D) Base heat flux and gas temperature comparison between Loci-CHEM and RAMP2 modeling approaches.

8.2.4 Boundary Layer Flow Physics

It is made obvious that changing the nozzle Iwall thermal boundary layer profile will result in different base heating characteristics. However, this boundary layer only makes a small fraction (<1%) of the entire nozzle mass flow rate. As a result, supporting flow physics to corroborate this observation are needed. It can be seen from Figure 12 that the Iwall boundary layer flow expands through the Prandtl-Meyer expansion waves into the wake region between the four nozzles (2 depicted in Figure 12). This low kinetic energy flow cannot pass the large pressure gradients developed by the Type I oblique shock-shock interactions from the adjacent plume jet shock boundaries. This results in the rebounding of the boundary layer flow toward the vehicle base and a downstream supersonic inviscid core as shown in Figure 12. It can be seen that the core plume flows downstream of the nozzle exit. This observation is also qualitatively supported by the NASA Space Shuttle base heating studies (Reference 20). This provides a clear picture as to how the thermal boundary layer profiles affects base heating.

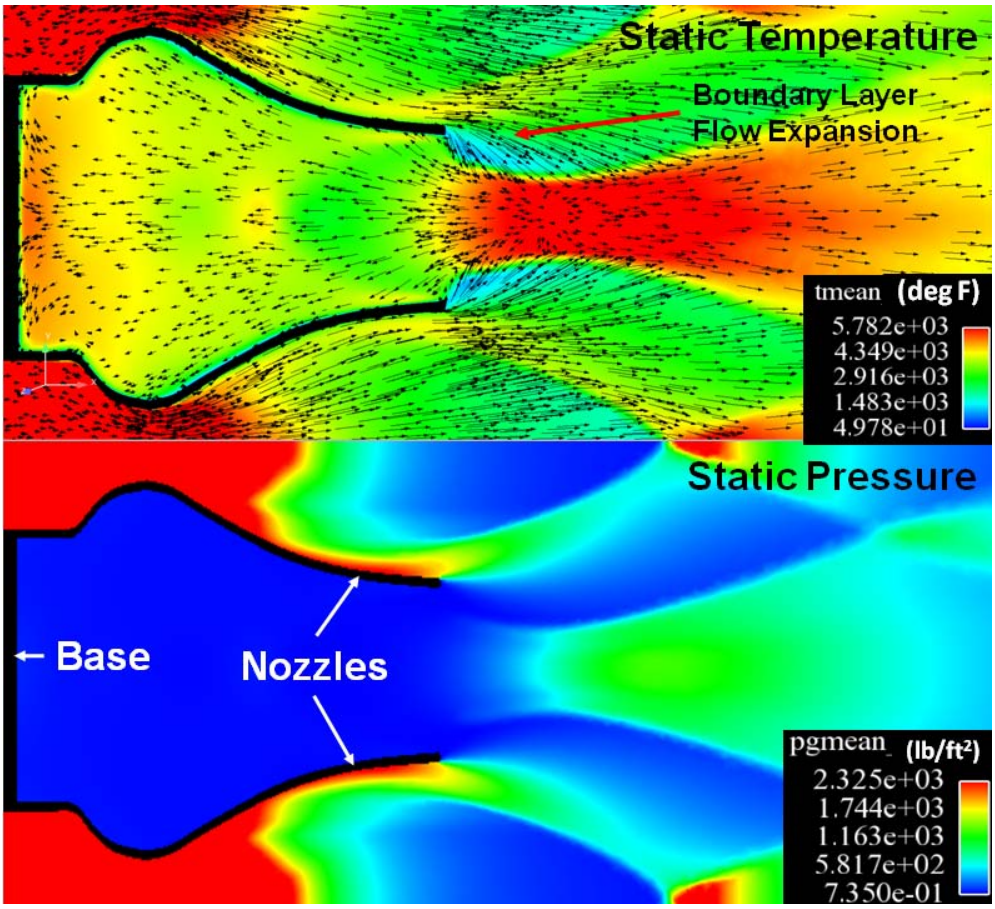

Figure 12. Base flow region. (Top) Velocity vector profiles overlaid over a mean static temperature contour plot for a simulated high altitude; (Bottom) Mean static pressure contour

8.3 Recovery Shock and Recirculation Zones

The rebounded inner nozzle wall boundary layer flow from the four nozzles results in either a subsonic or supersonic updraft plume as shown in Figure 7. It can be seen that at simulated low altitude cases, the updraft plume that interacts with the base is subsonic while the plume is supersonic at high altitude cases. At the low altitude case, the jet expansion angle is much smaller than for the high altitude case and this prevents full choking of the exhaust plume, resulting in a decrease in the updraft plume velocity and an increase in the downward aspirating jet velocity component. This is observed to be within the transitional-flow regime. This effect along with higher ambient pressure within the base region leads to stronger shear forces to decelerate the flow. This produces a free turbulent shear jet with a characteristic steady Gaussian-type pressure distribution. The aspirating jet leads to entrainment of the freestream gases to downstream of the nozzles, resulting in a decrease in the base pressure. Loci-CHEM slightly over-predicts entrainment as observed in Figure 4 and this effect

is more pronounced at simulated low altitude case due to a higher freestream density. This is also observed for Loci-CHEM's numerical base heating study of the Saturn V (Reference 16).

However, for the high altitude case, the dynamics are more complex due to full-choking of the exhaust plume near the base region (Figure 13) which blocks the freestream air from exiting the base region. This is characterized to be within the recirculating-flow regime. The rebounding Iwall boundary layer flow expands supersonically into the low ambient pressure base region environment. The supersonic updraft plume impinges at the center of the base and leads to the formation of a recovery shock and a wall jet (Figure 13). The recovery shock is a normal shock wave that is detached a few inches from the center base plate. This leads to large peaks in both the heat flux and static pressure at the base center as shown in Figures 6 and 4 and their magnitudes are a function of the strength of the normal shock wave and specific heat ratio. This is not as pronounced for the low altitude case, due to its' inability to form a recovery shock. The wall jet propagates from the recovery tail shocks along the base to supersonic speeds; demonstrates compression and expansion regimes and decays as a function of axial distance. It can be seen in Figure 13 that low-pressure and velocity recirculation zones surround the updraft plume. This is further confirmed by taking the curl of the velocity vector (vorticity), $\nabla \times \vec{u}$, of the numerical solution and observing high vorticity within this region.

The recovery shock's movement and changing orientation leads to significant pressure and heat flux perturbations. From time-accurate numerical simulations, the shock rotates along the center base at a fixed frequency. This leads to a larger validation uncertainty in the base pressure and heat flux solutions as compared to the low altitude case as shown in Figures 16 and 18. These oscillations and movement of the recovery shock occur due to momentum balancing between the high pressure updraft plume and the surrounding low-pressure moving recirculation zones. Similar aerophysics were observed in the base flow region for the NASA Saturn V Launch Vehicle.

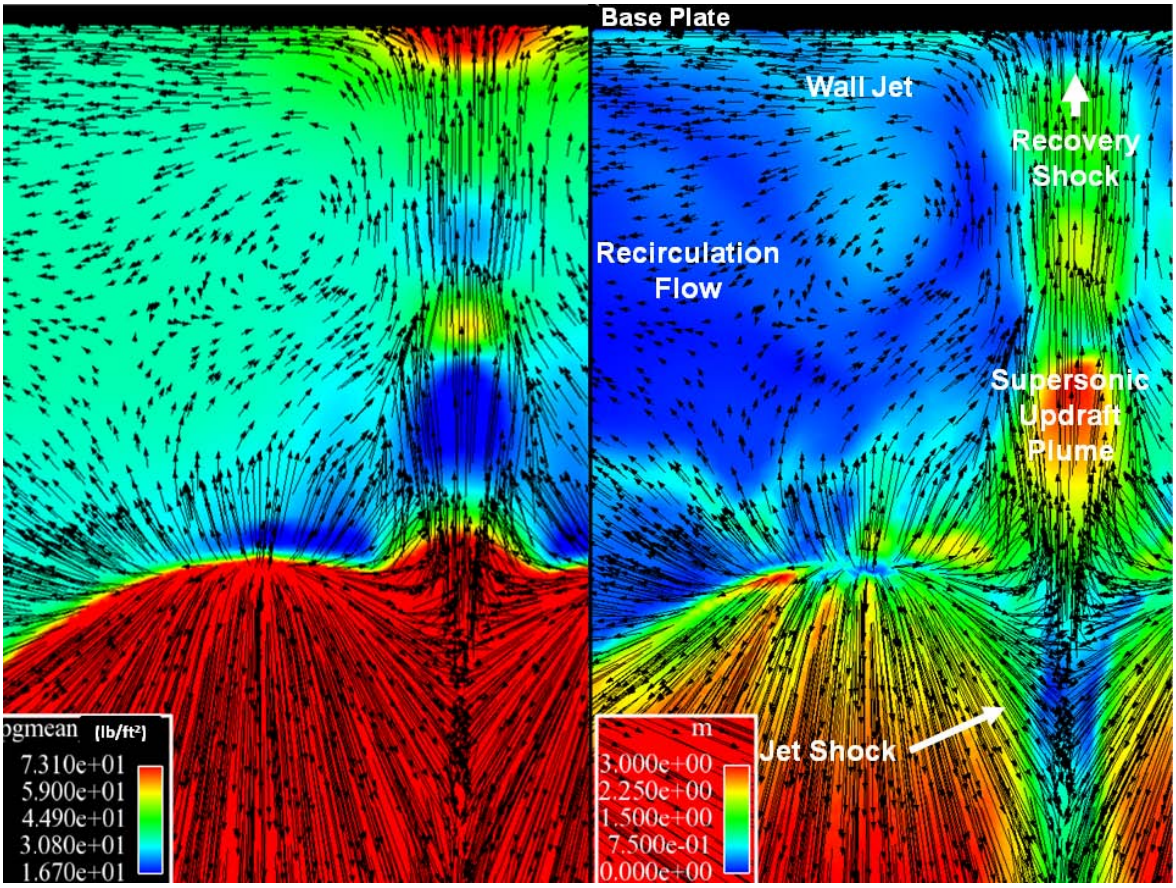

Figure 13. Sectional plane taken between the pair of nozzles within the base flow region. (Left) Velocity vectors overlaid on mean static pressure contours of the updraft plume impingement on the base at simulated high altitude; (Right) Velocity vectors overlaid on Mach contours

8.4 Plume-Induced Flow Separation (PIFS)

PIFS is another flow structure that is observed during the base recirculating-flow regime and it partially affects both base heating and base drag. Recirculation and flow separation are important to accurately predict from an aerodynamics and aerothermodynamics perspective. The launch vehicle experiences a change in aerodynamic forces and moments as a consequence to flow separation occurring at the base. Aerodynamic heating can be accentuated within the recirculation regions or zones of separation. As the plume expansion ratio increases (low to high altitude), this difference between the recirculatory plume pressure and the ambient pressure increases due to the influence of stronger wall jets. This pushes the recirculation zone outward (Figure 7) and promotes the separation of the attached freestream from the surface of the vehicle. This is known as Plume-Induced Flow Separation (PIFS). These recirculation zones can increase the base drag and lead to side load oscillations

if there is flow asymmetry. PIFS is somewhat observed for the high altitude case in the base region between the rocket motors (not shown).

8.5 Chemical Reactions and Afterburning

This section will provide insight on how chemical reactions may influence base heating characteristics. By implementing Ten-See Wang's RP-1/LOX chemistry model (Reference 11) within the interior section of the nozzles, the effects of the chemical reactions were observed within the Iwall boundary layer. Water and carbon dioxide are stable along the boundary layer due to a cool wall temperature. The mass fraction contours in Figure 14 show that the carbon monoxide oxidizes to form carbon dioxide across the shock due to a static temperature jump. Carbon dioxide molecules break down within the boundary layer when the recovery temperature is high as in the adiabatic wall case. Change in the plume composition due to internal nozzle shocks or Iwall temperature conditions leads to different transport and thermodynamic properties within the boundary layer. Soot at 1-2% of the total mass flow was also observed within the nozzle inner and outer wall boundary layers.

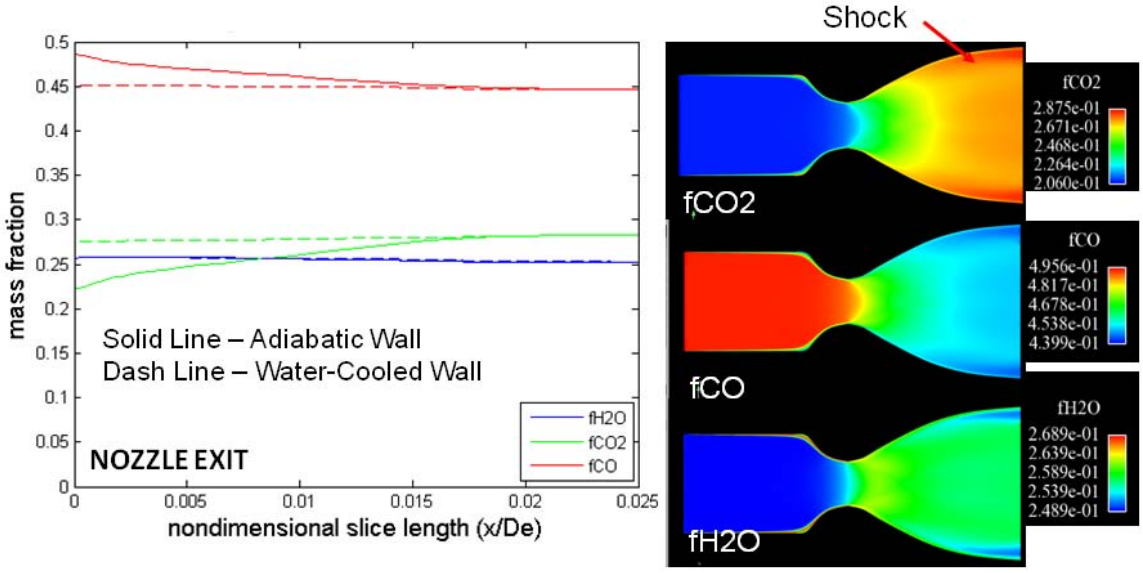

Figure 14. (Left) Mass fraction vs. nondimensional slice length near the nozzle exit within the nozzle inner wall boundary layer; (Right) Mass fraction contours for the major species within the nozzle interior

Another region where chemical reactions play a direct role in base heating is the effect of afterburning. The ambient gases in particular oxygen entrains into the base region. This is observed by mapping inert nitrogen gas within the base region. Since combustion reaction in our case is not stoichiometric, there are residual hydrocarbons and carbon molecules that mainly reside within the

boundary layer due to low wall temperatures and high molecular weights. As a result, at relatively high plume temperatures and the mixing of carbon and oxygen leads to combustion and release of chemical energy within the updraft plume. This can be observed in Figure 15 where the static temperatures are higher in the base region by ~900 deg F between the frozen flow and finite-rate chemistry solutions. This is further confirmed by taking the divergence of the water mass flux at each cell within the numerical domain. Afterburning leads to a substantial increase in the base center heat flux of ~15 BTU/ft^2-s for the low altitude case and ~10 BTU/ft^2-s for the high altitude case (Figure 6). This effect is more pronounced at low altitude due to a higher number density of oxygen molecules. Afterburning is also observed within the jet shock's shear layer downstream of the nozzle exit.

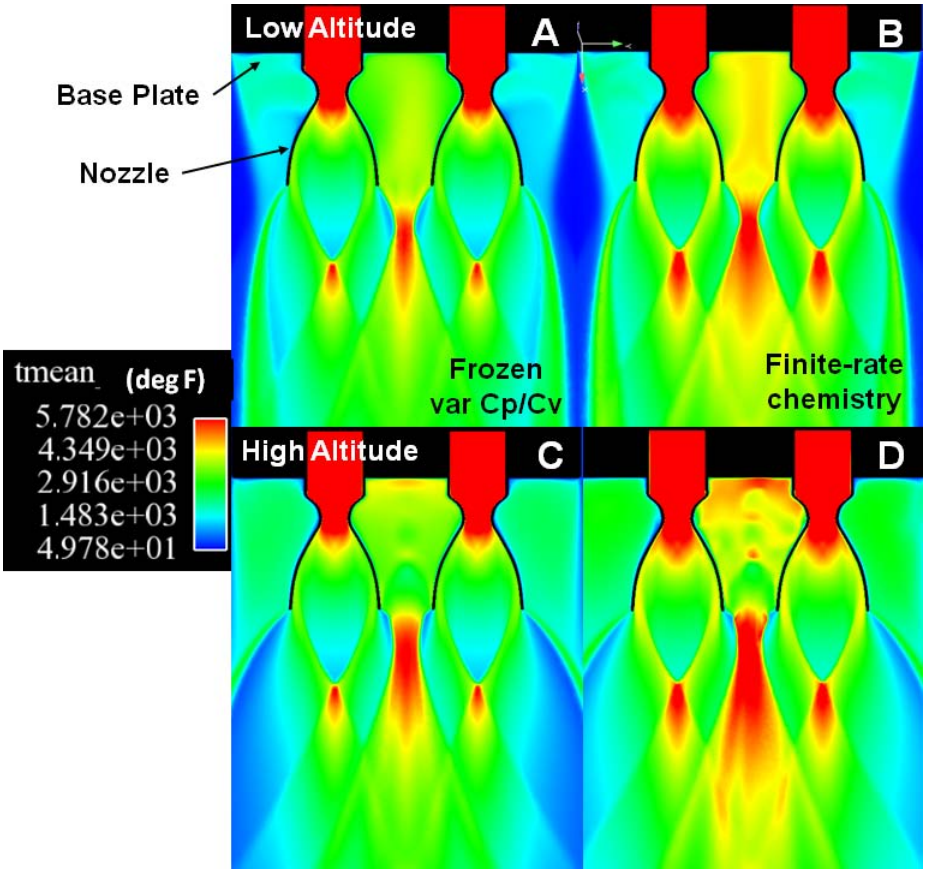

Figure 15. Mean static temperature contours between frozen and finite-rate chemistry solutions with 800 deg F Iwall conditions at (A and B) simulated low altitude and (C and D) simulated high altitude

9.0 Uncertainty Analyses

Before we proceed to determine the uncertainty analyses and if the solutions are validated, a qualitative appreciation of the challenges and difficulties in modeling these test cases should be presented. There are many important boundary conditions omitted from the test report (Reference 7) such as the nozzle inner and outer wall temperature distribution. This results in large uncertainties in the base heat flux and gas temperature profiles. The geometries of the sting, fuel and oxidizer injectors and missile forebody such as length, nose cone radius and general profile were not recorded in the document. This can lead to uncertainties in the ambient pressure near the base region especially for higher number density mediums. The minor contribution of plume radiation to the heat flux was not measured. However, the NASA TND-1093 test is one of the few reports which documents heat flux, pressure and gas temperature for various rocket motor designs and configurations.

To determine if the base heating numerical solutions obtained by Loci-CHEM can be considered validated or if the measurement data is between the $\pm U_V$, validation uncertainty profiles, two parameters are calculated: (1) numerical solution uncertainty (U_{SN}) and (2) measurement uncertainty (U_D) assuming no bias. U_D was determined from other literature (References 17-19), because the test report did not document the measurement uncertainty. U_D is denoted by blue error bars overlaid on the test data (blue circles). The $\pm U_V$ profiles are indicated by the green dashed lines and calculated by Equation 1. It is important to note that a one sigma confidence level was applied to these analyses. All uncertainty analyses were done with the highest fidelity models which included finite-rate chemistry and accurate Iwall temperature boundary conditions. As shown in Figures 16-18, most of the solutions are considered validated to the U_V level without any implied programmatic tolerance. However, the base gas temperature distribution at high altitude and base pressure distribution at low altitude did not fall into this category. The possible reasons are discussed in the Results Section.

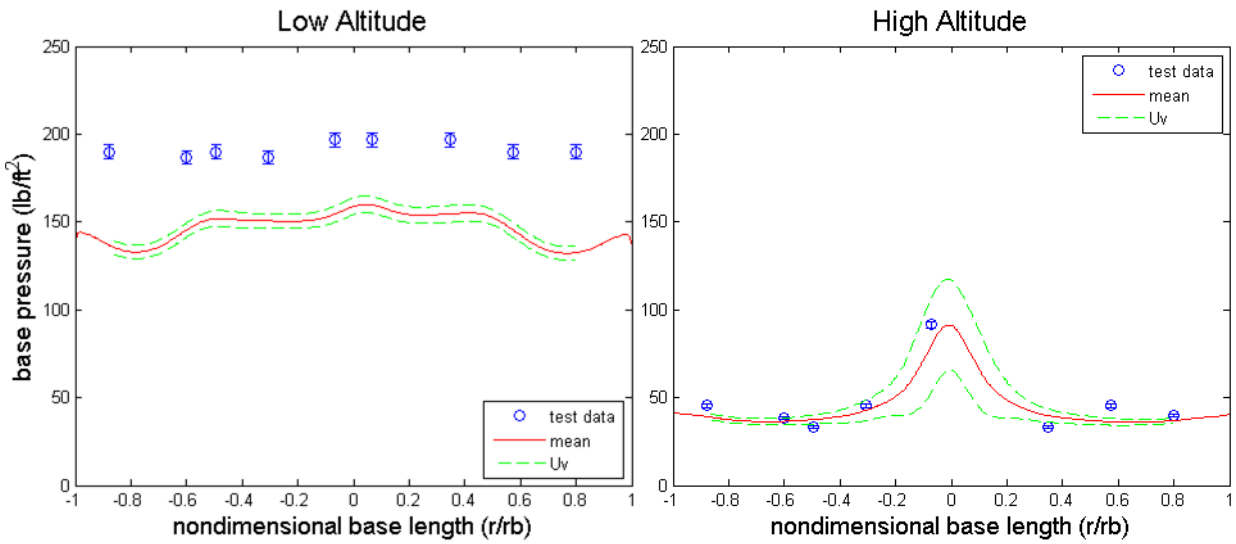

Figure 16. Validation uncertainty bands (green dashed lines) for base pressure at simulated low (left) and high (right) altitudes

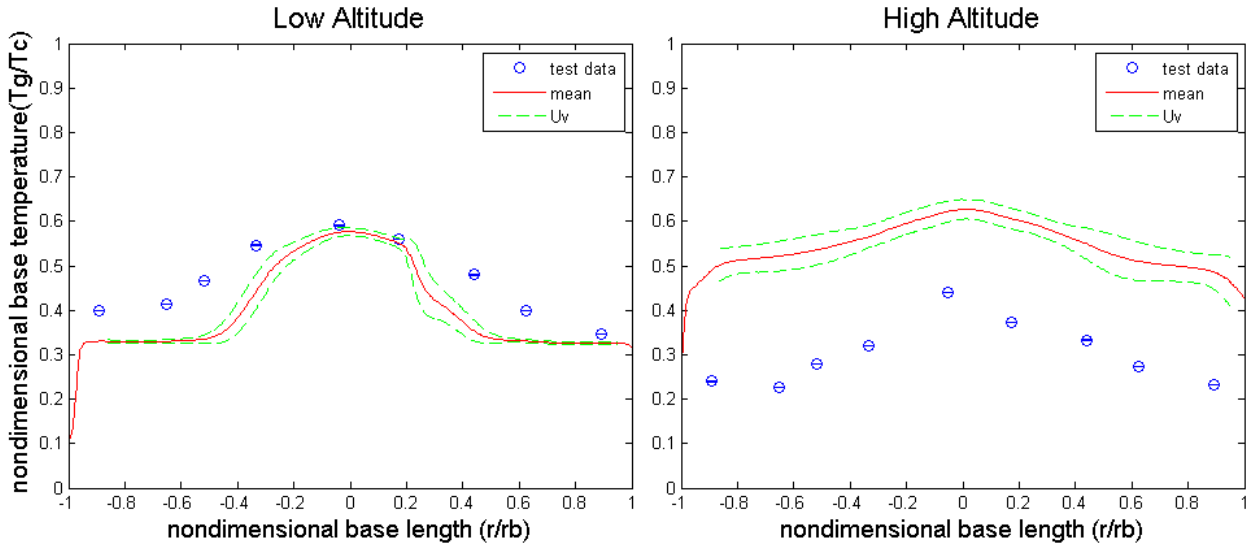

Figure 17. Validation uncertainty bands (green dashed lines) for nondimensional base gas temperature at simulated low (left) and high (right) altitudes

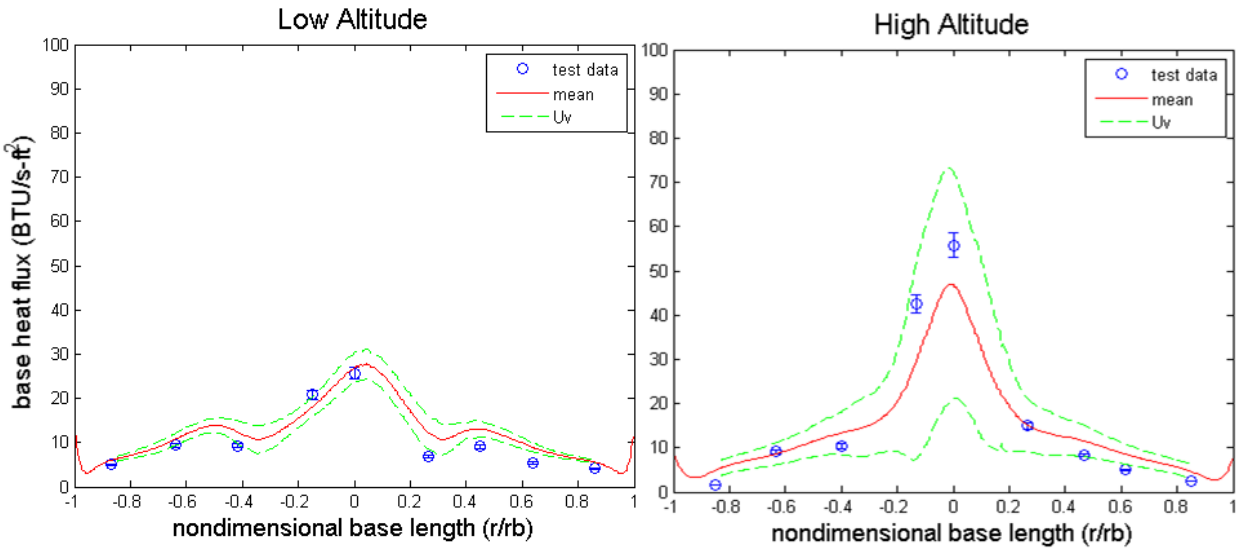

Figure 18. Validation uncertainty bands (green dashed lines) for base heat flux at simulated low (left) and high (right) altitudes

10.0 Error Analyses

The error factor quantitatively determines the fraction of error (or deviation) in the numerical solution as compared to the test data. This factor is not a statistical quantity such as U_v and it does not provide any insight on whether the solution is validated. The equation to determine this factor is given by the following:

$$f_{ERROR} = \frac{(NS - D)}{D} \qquad (11)$$

Where NS and D are defined earlier and f_{ERROR} is the deviation fraction from the measurement (D) value. The bar charts in Figures 19 and 20 provide a quick assessment of how well the numerical solutions of various models compare to the test data. Error factor bar charts were not provided for the base pressure due to minor deviations between each model.

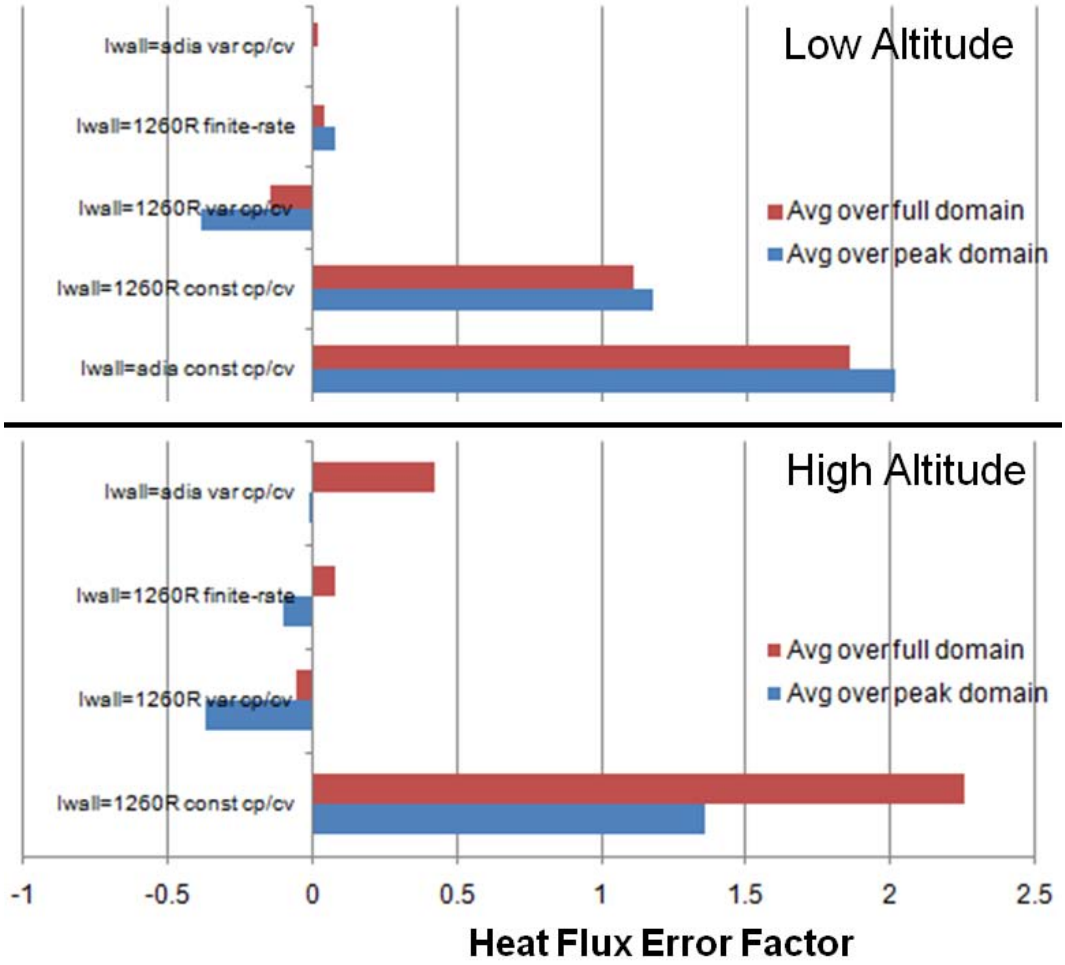

Figure 19. Bar charts of the heat flux error factor for the various cases modeled at both simulated high and low altitudes (Iwall temperature of 1260 deg R equals 800 deg F)

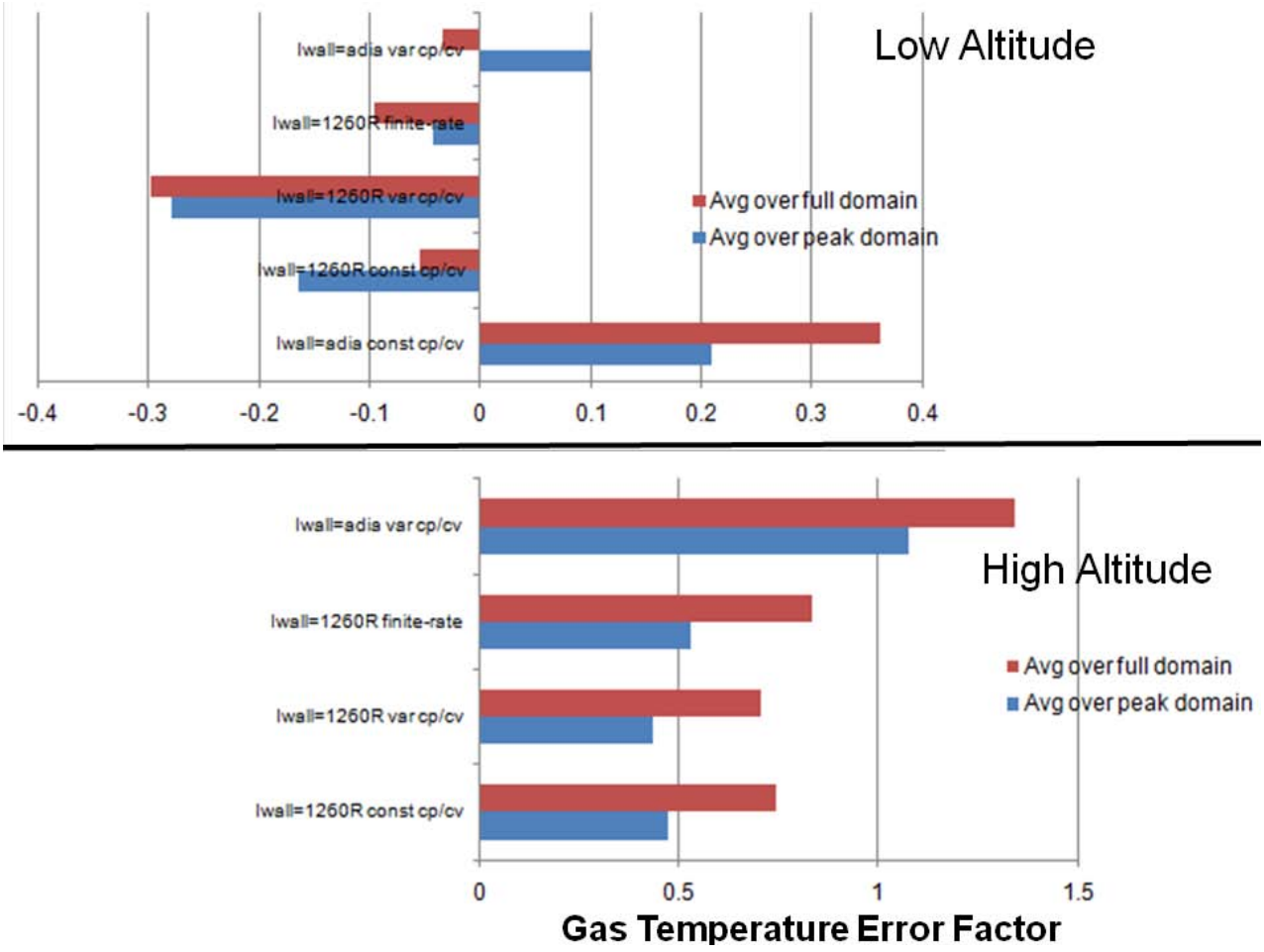

Figure 20. Bar charts of the gas temperature error factor for the various cases modeled at both simulated high and low altitudes (Iwall temperature of 1260 deg R equals 800 deg F)

11.0 Conclusions

The sensitivity study of the 4-cluster rocket motor configuration provided insight into new and existing modeling approaches, new findings into the aerophysics of base heating flows and validation of numerical simulations. It was determined through this study that base heating is most sensitive to Iwall temperature boundary conditions and thermodynamic and chemistry numerical models. Our study shows that the Iwall thermal boundary layer is the main driver in accurately predicting base heating characteristics. The aerophysics of this thermal boundary layer is significantly influenced by the Iwall temperature, plume specific energy, plume expansion ratio, and boundary layer chemical reactions. Other important factors that significantly influence base heating are the recovery shock dynamics and afterburning especially within the transitional and recirculating-flow regimes. The Twall thermal boundary layer and turbulence

modeling showed less sensitivity to base heating. Barring a few test complications, validation of high fidelity numerical simulations were mostly achieved for base heat flux, pressure and temperature profiles. Implementing accurate boundary conditions, thermodynamic models and finite-rate chemistry models were required for the numerical solutions to achieve validation.

12.0 Acknowledgements

We would like to thank the technical support of Mark G. D'Agostino, Branch Chief, and Brandon L. Mobley (Qualis Corporation) of the NASA MSFC Aerosciences Branch.

References

1. Luke, E.A. et al. (2010), CHEM 3.2: A finite-rate viscous chemistry solver – the user guide, NASA SBIR Document.

2. Tashakkor, S. and F. Canabal (2011), Loci-CHEM computational fluid dynamics code validation for predicting launch vehicle aerodynamic heating, NASA MSFC Memorandum of Record.

3. Canabal, F., J. Mishtawy and J. West (2008), Loci-CHEM computational fluid dynamics code validation for predicting plume impingement pressure and heating, NASA MSFC Memorandum of Record.

4. Goethert, B.H. (1960), Base flow characteristics of missiles with cluster-rocket exhausts, IAS Paper No. 60-89.

5. Morris, J.A. and A.L. Cannell (1961), Base recirculation of a 1/10-scale Saturn S-IV Stage at simulated altitudes above 142,000 feet. AEDC-TN-61-102 Report.

6. Roach, P.J. (1998), *Verification and Validation in Computational Science and Engineering*, New York: Hermosa Publishers.

7. Musial, N.T. and J.J. Ward (1961) Base flow characteristics for several four-clustered rocket configurations at Mach numbers from 2.0 to 3.5, NASA TND-1093.

8. Nallasamy, R. et al. (2008), Numerical simulations of the base flow and heat transfer characteristics of a four-nozzle clustered rocket engine, 40th AIAA Thermophysics Conference, Seattle, WA.

9. http://www.simcenter.msstate.edu/docs/solidmesh

10. http://www.simcenter.msstate.edu/docs/aflr3

11. Wang, T.S. (2001), Thermophysics characterization of kerosene combustion, AIAA Journal of Thermophysics and Heat Transfer, Vol. 42, No.2

12. Menter, F.R. (1994), Two-equation eddy-viscosity turbulence models for engineering applications, AIAA Journal, Vol. 32, No. 8.

13. Smith, S.D. (1984), High-altitude chemically reacting gas particle mixtures Volume III – Computer Code User's and Applications Manual, NASA CR – NAS9-16256.

14. Gordon, S. and B.J. McBride (1971), Computer program for calculation of complex chemical equilibrium compositions, rocket performance, incident and reflected shocks and Chapman-Jouguet detonations, NASA SP-273.

15. Vincenti, W.G. and C.H. Kruger (1965), *Introduction to Physical Gas Dynamics*, New York: John Wiley & Sons, Inc.

16. Mobley, B.L., Tashakkor, S.B., Mehta, M. and Canabal, F. (2011), Launch vehicle base heating CFD validation status, NASA MSFC EV01 Status Presentation.

17. Omega Product On-line manual: http://www.omega.com

18. Thermo-Electric Product On-line manual: http://www.thermo-electric.nl

19. Kidd, C.T. (1981), High heat flux measurements and experimental calibrations/characterizations, AEDC – N93-13663.

20. Reardon, J.E., R.L. Bender and R.D. Haynes (1992), Space Shuttle Plume Methodology Base Heating Data Book: Series 1 – Ground and Flight Test Data, REMTECH Inc., Report ID: M2L8XXH-453039G.

21. Sutton, G.P. and O. Biblarz (2001), *Rocket Propulsion Elements*, New York: John Wiley & Sons, Inc.

22. Burt, J.D. and I.D. Boyd (2007), High-altitude plume simulations for solid propellant rocket, AIAA Journal, Vol. 45, No. 12.

23.http://www.engineering.com/Library/ArticlesPage/tabid/85/articleType/ArticleView/articleId/151/Emissivity.aspx

24. Pastor, E. et al. (2002), Experimental methodology for characterizing flame emissivity of small scale forest fires using infrared thermography techniques, Forest Fire Research & Wildlife Fire Safety, Millpress, Rotterdam, ISBN 90-77017-72-0.

25. Burley, R.R. and D.E. Harrington (1987) Experimental evaluation of blockage ratio and plenum evacuation system flow effects on pressure distribution for bodies of revolution in 0.1 scale model test section of NASA Lewis Research Center's Proposed Altitude Wind Tunnel, NASA TP-2702.

BASE HEATING SENSITIVITY STUDY FOR A 4-CLUSTER ROCKET MOTOR CONFIGURATION IN SUPERSONIC FREESTREAM

Manish Mehta, Ph.D., Francisco Canabal, Ph.D.,
Scott B. Tashakkor, P.E. and Sheldon D. Smith

Aerosciences Branch
NASA Marshall Space Flight Center

Presented By

Manish Mehta

Thermal & Fluids Analysis Workshop
TFAWS 2011
August 15-19, 2011
NASA Langley Research Center
Newport News, VA

Road Map

- Introduction
  - Motivation
  - General Base Flow Physics
- Test Methodology
- Numerical Methodology
- Results
  - Flow Field
  - Base Heating Characteristics
- Discussion
  - Sensitivity Study
  - Aerophysics
  - Validation Study
- Conclusion

Motivation

- Base heating prediction is critical for launch vehicle (LV) mission success.
  - Prevents base plate and base instrumentation damage
  - Decreases design margin, decreases cost and improves LV performance
- Current prediction tool: semi-empirical methodology

  Drawbacks:
  - Envelopes environments over broad zones
  - Dependent on the limitation of the data base
  - Cannot provide physics, surface and volumetric distributions
- Future prediction tool: computational fluid dynamics (CFD)
  - Due to changes in LV configuration and rocket motors, a physically-based approach is necessary for design of the next-generation LVs
  - Two studies are needed to make CFD a credible design tool for base heating applications
    - Validation Study: determine if CFD can accurately describe the aerophysics and obtain validated solutions
    - Sensitivity Study: determine how CFD solutions responds to changing parameters to improve modeling approaches and provides insight into the aerophysics

Base Flow Field

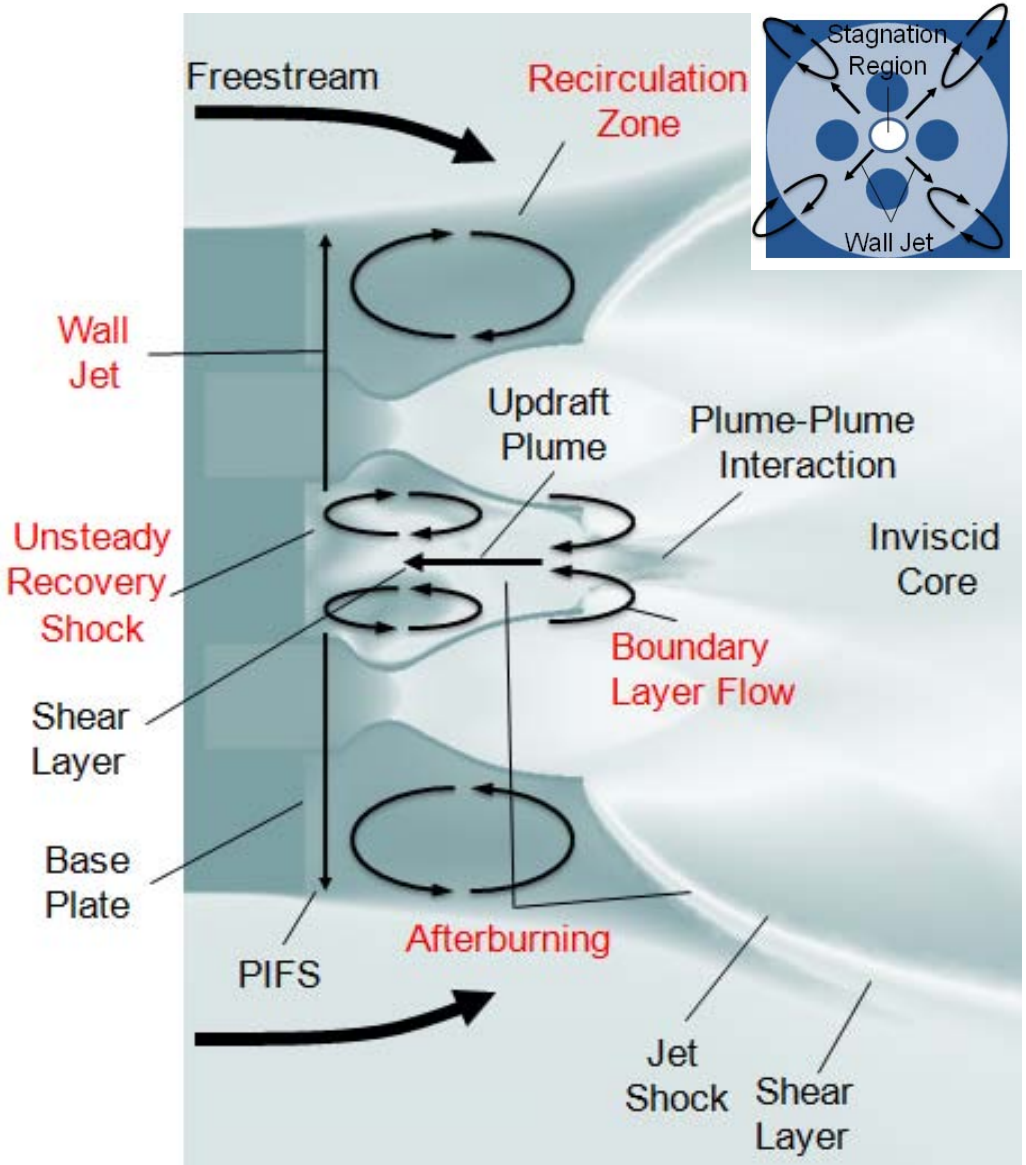

Limited numerical and analytical studies have been conducted to fully characterize multi-plume base heating.

For the following reasons:
1. Complex
2. Unsteady
3. Many interacting flow features
4. Leads to many different trends, distributions and deltas

Base Flow Regimes:

Aspirating – Freestream air is entrained by the non-interacting rocket plumes

Transitional – slight interactions by adjacent plumes leads to updraft plume component and downward aspirating jet

Recirculating – large interactions by highly expansive plumes leads to predominantly an updraft plume

Test Methodology

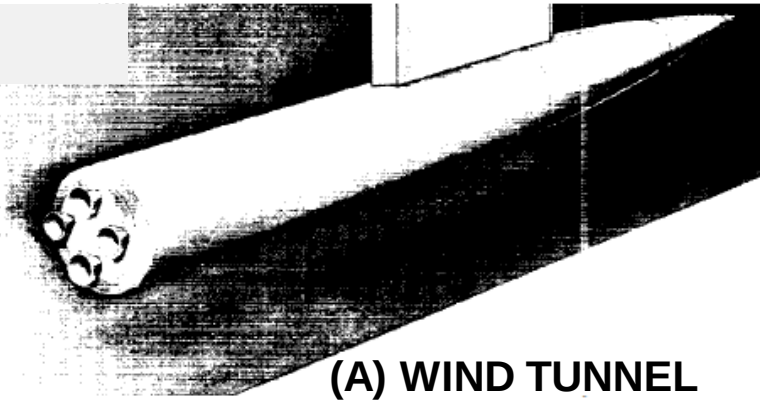

(A) WIND TUNNEL

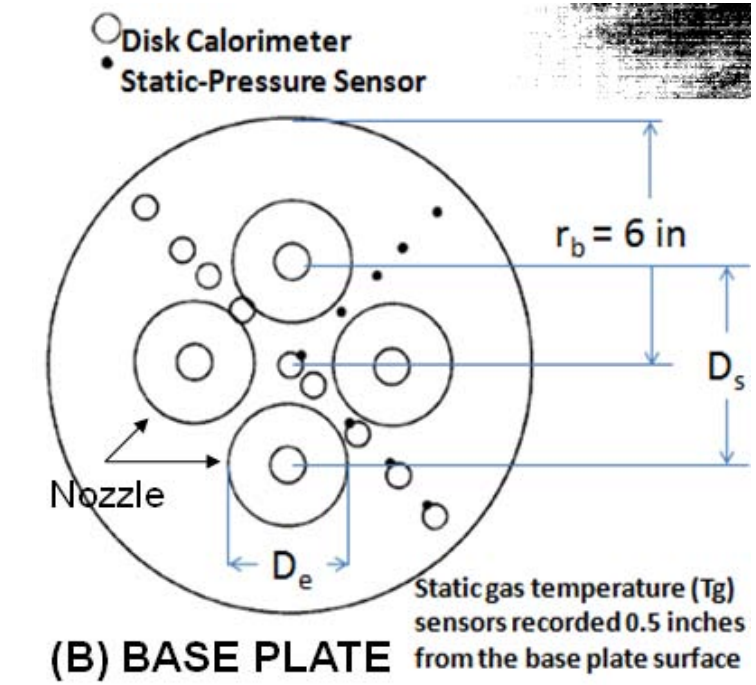

(B) BASE PLATE

Musial and Ward **NASA Lewis Supersonic Wind Tunnel (SWT) Rocket Tests** characterized multi-plume base heating by varying the nozzle spacing and extensions and the ambient atmospheric pressure

Firing of four 500 lbf JP-4/LOX rocket motors with nozzle area ratio of 12 for 10 sec in Mach ~2.75 freestream air

Calorimeters, thermocouples and pressure transducers instrumented on the base plate

Nozzle inner wall (Iwall) temperature, missile forebody dimensions and radiation heat flux were not recorded

Numerical Methodology

Modeling

- 5 grids generated and 35 numerical simulations modeled
- 3-D Geometry & Surface Mesh – SolidMesh
- Volume & Boundary Layer Grid Generation – AFLR3
- CFD Solver – Loci-CHEM
- Engineering Code – RAMP2-BLIMPJ
- Post-processor – Ensight & in-house MATLAB Code

Geometry Configuration

- D_s = Nozzle spacing = 1.57 D_e
- L = Nozzle extension = 1.63 D_e
- D_e = Nozzle exit diameter = 2.94 in

Mesh Generation

- 30 million unstructured cells
- Highest resolution in nozzle interior, boundary layer and base flow regions
- High resolution in plume wake
- High quality grid

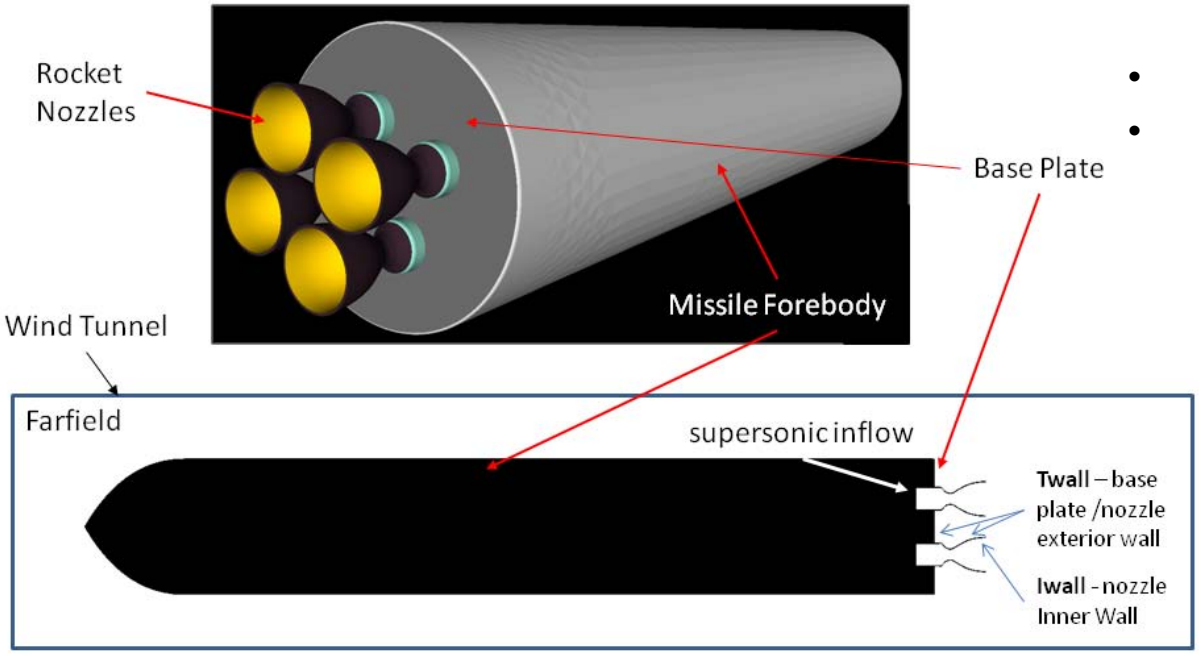

Adiabatic and varying Iwall temperature viscous wall conditions

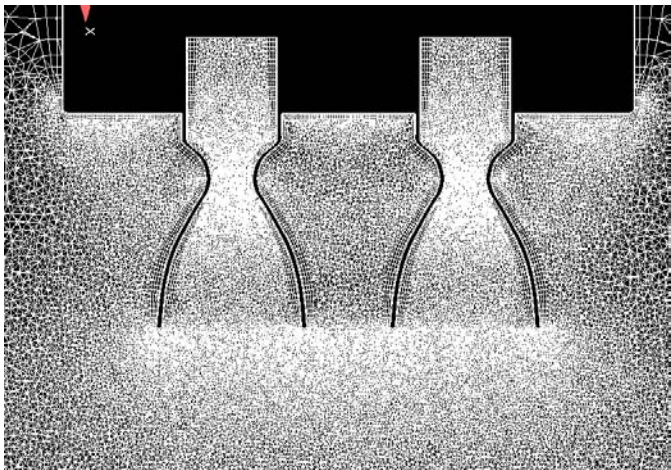

Boundary and Initial Conditions

Boundary and initial conditions of the NASA Lewis SWT, rocket motor thrust chamber and nozzle exit.

Parameters	Simulated High Altitude	Simulated Low Altitude	
P_∞ - ambient (lb/ft^2)	35	255	Wind Tunnel
T_∞ (F)	76.4	76.4	
M_∞	2.75	2.75	
Simulated Altitude (ft)	90,700	48,900	
P_c – thrust chamber (lb/ft^2)	86,400	86,400	Thrust Chamber
T_c (F)	5786	5786	
Re	5×10^6	5×10^6	Nozzle Exit
Jet expansion ratio	24.7	3.4	

Sensitivity Modeling Parameters

Varied the thermodynamic and chemistry models and Iwall temperature conditions. Twall conditions and turbulence modeling show to be relatively insensitive.

Test Cases	Twall (F) (Nozzle Outer Wall & Base Plate)	Iwall (F) (Nozzle Inner Wall)	Comments
Variable Cp/Cv	150	800	Equivalent plume species with varying c_p as a function of temperature. c_p (T) is empirically derived by the NASA Lewis CEC Library (Reference 14). Defined as frozen flow.
Cp/Cv = 1.15	150	800	Equivalent plume species with constant c_p determined at the thrust chamber section from the NASA Lewis CEC.
Finite-rate chemistry	150	800	10 major plume species are modeled with empirically derived c_p(T) and 17 major chemical reactions for RP-1/LOX are modeled with empirically derived reaction rates calculated from the Arrhenius eqn.
Iwall=adia, Variable Cp/Cv	150	Adiabatic	Similar thermodynamic model as Variable Cp/Cv. Nozzle inner wall (Iwall) is adiabatic.
Iwall=adia, Cp/Cv=1.15	150	Adiabatic	Similar thermodynamic model as Cp/Cv =1.15. Nozzle inner wall (Iwall) is adiabatic.
Test Data	150	Unknown	

Highest Fidelity Simulation

Flow Field

Plume structures are different between two altitude regimes because this is a function of the ambient shear and pressure forces on the shock layer.

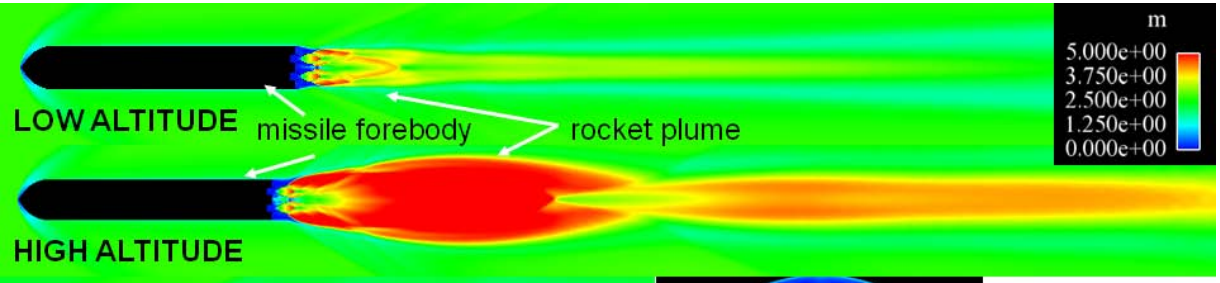

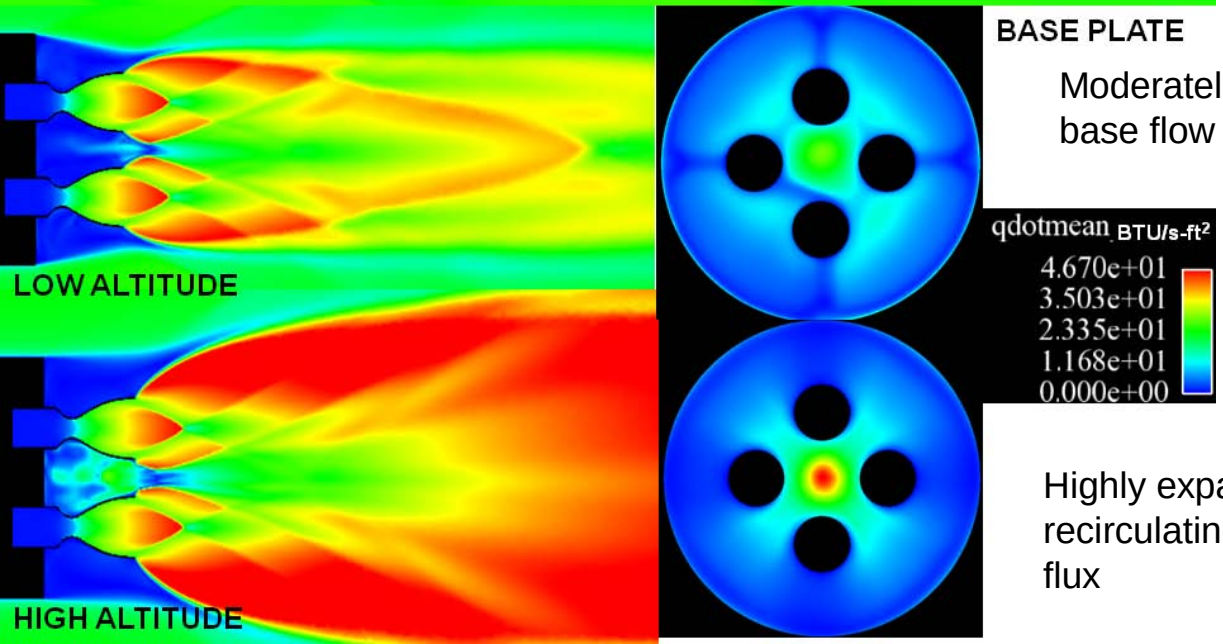

Moderately expansive plumes lead to transitional base flow regime and low base heat flux

Highly expansive plumes lead to choked-recirculating base flow regime and high base heat flux

Base Pressure

Base pressure data shows good agreement (within 15%) for various modeling parameters.

Over-prediction of entrainment for highest fidelity solution (green curve) leads to decrease in base pressure for the simulated low altitude case.

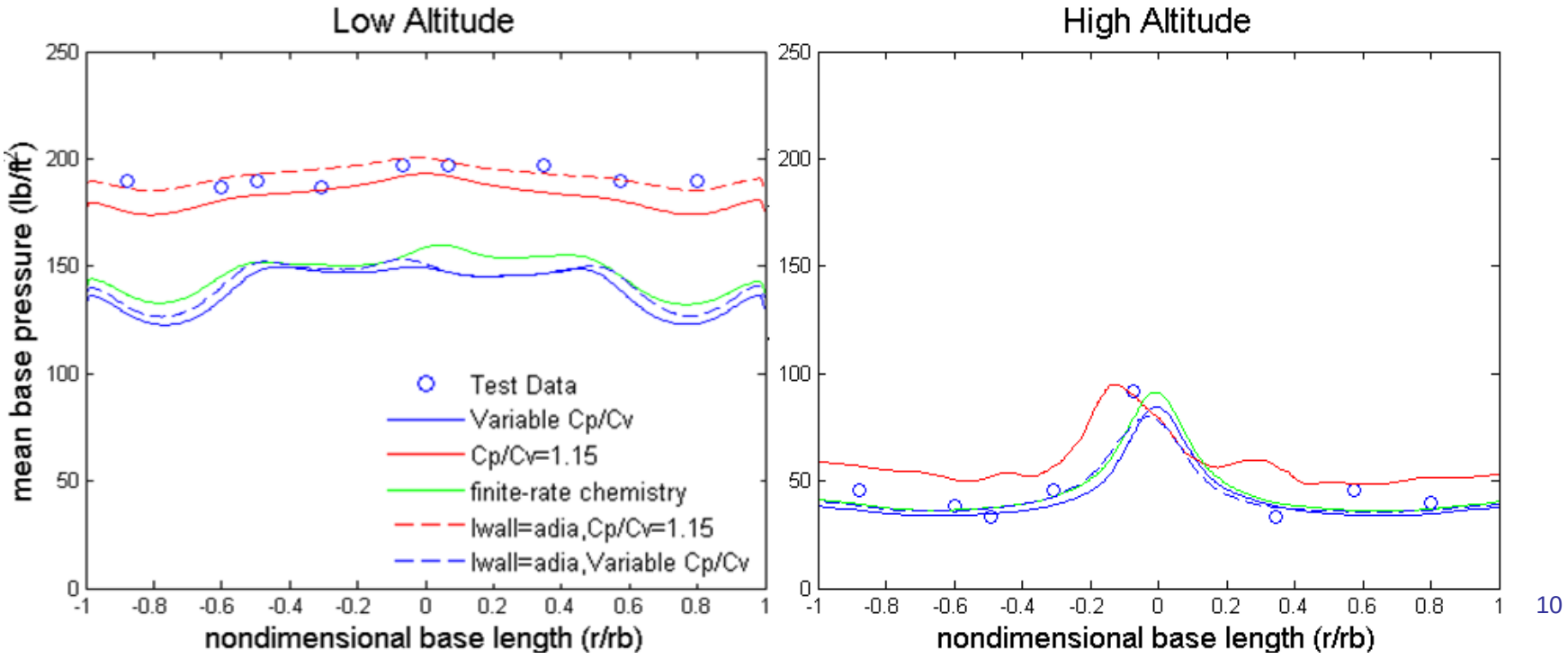

Base Gas Temperature

Base gas temperature data shows best agreement (within 50%) with highest fidelity solution (green curve).

Over-prediction of base gas temperature for high altitude case attributed to nozzle cooling and radiation losses.

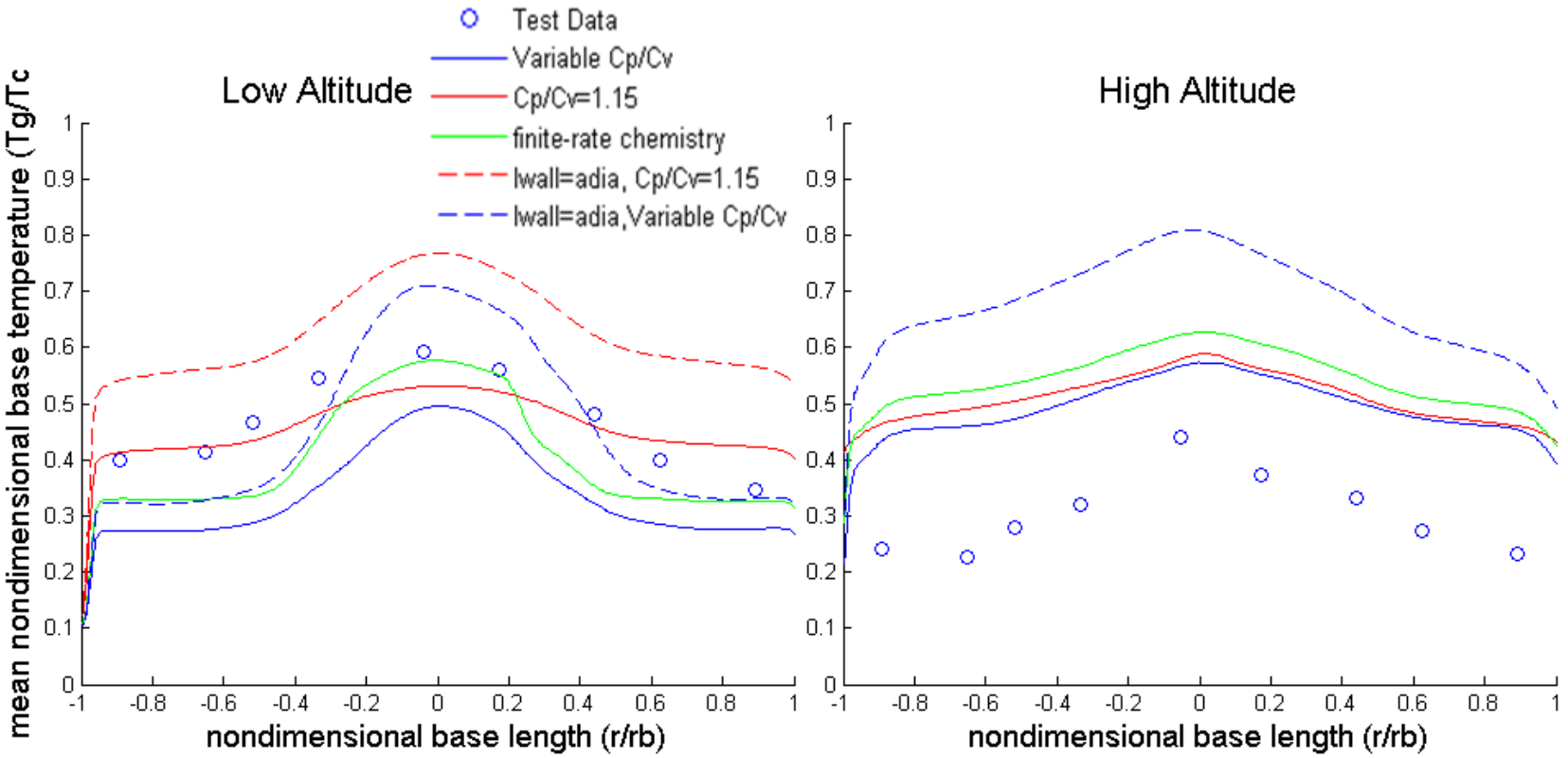

Base Heat Flux

Base heat flux data shows best agreement (within 10%) with highest fidelity solution (green curve).

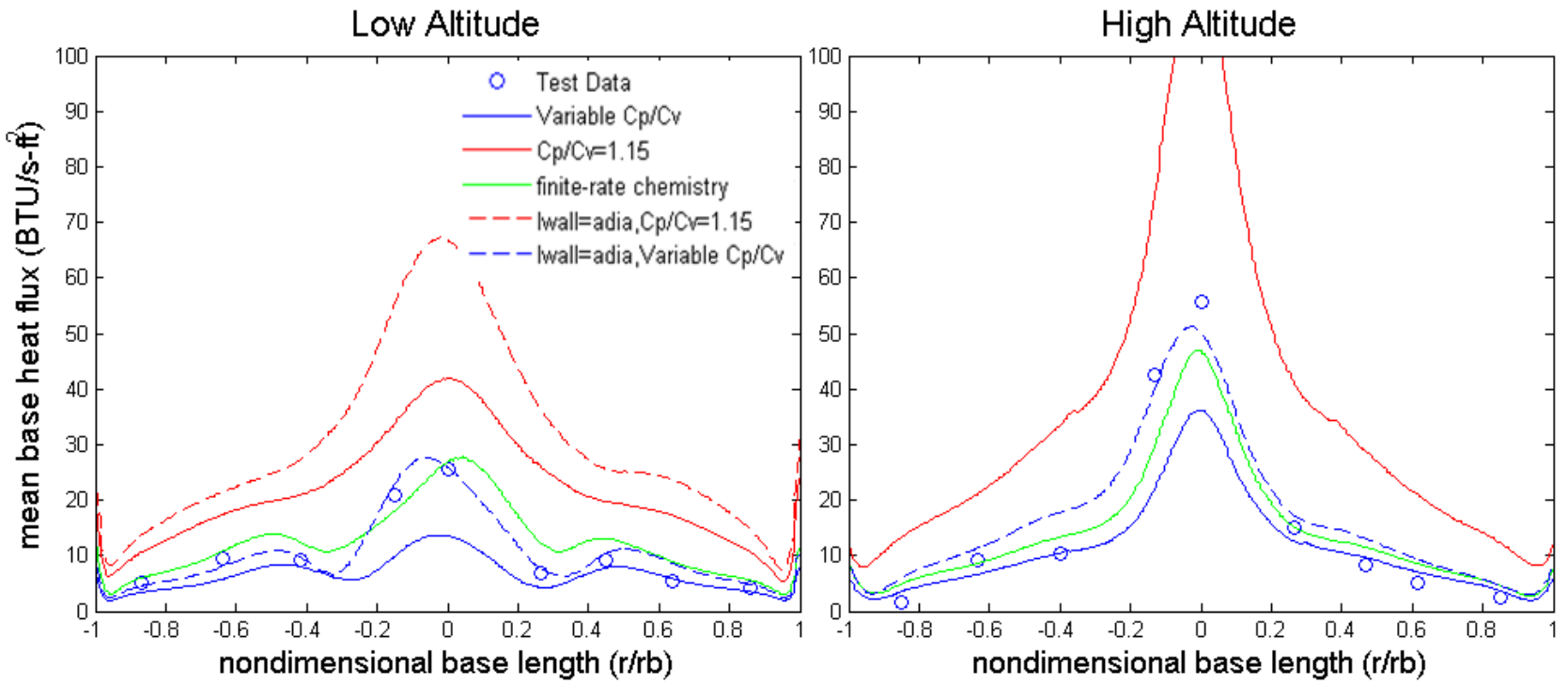

Iwall Temperature Sensitivity

20% increase in the areal-thermal boundary layer profile between the Iwall 800 deg F (blue curve) and adiabatic wall (green curve) boundary condition leads to an average increase of 70% in the base heat flux and 45% in the base gas temperature.

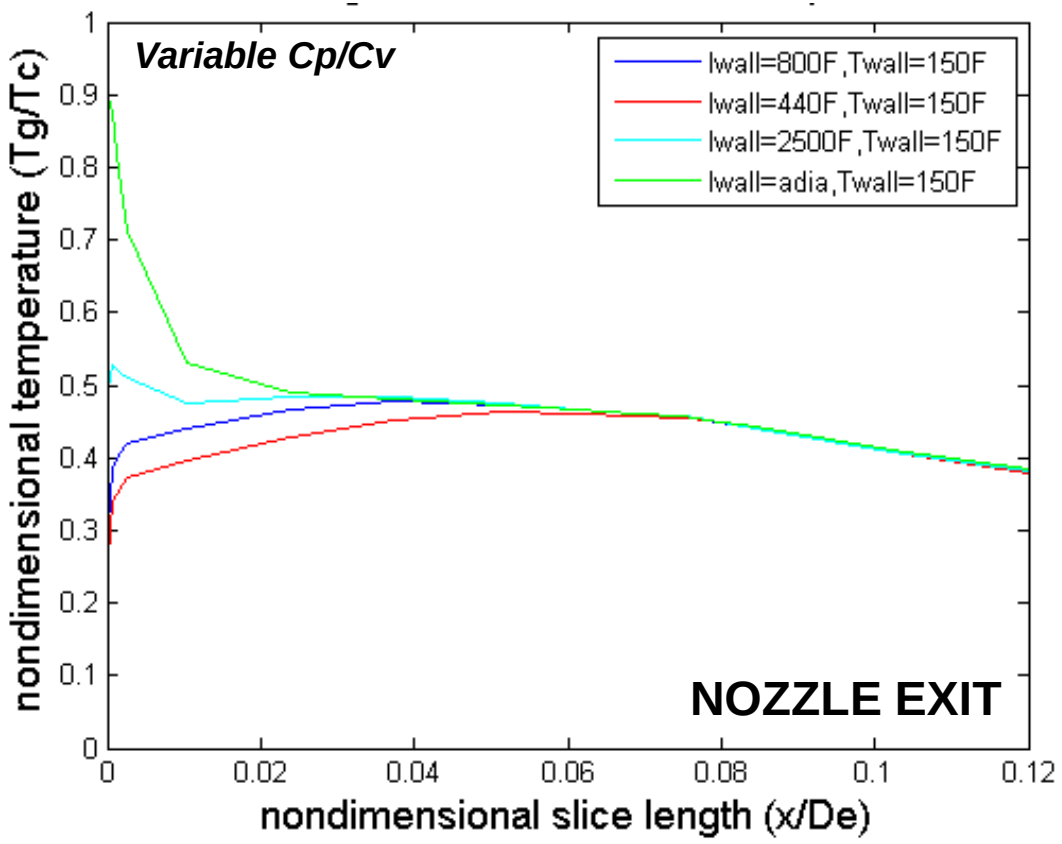

Adiabatic wall assumes no heat escape and results in artificially higher boundary layer temperatures and thermal energy for regenerative-cooled liquid rocket engines

Sensitivity of Thermodynamic and Chemistry Models

20% increase in the areal-thermal boundary layer profile between the finite-rate chemistry solution (green) and the frozen flow solution (blue) leads to an average increase of 60% in the base heat flux and 20% in the base gas temperature

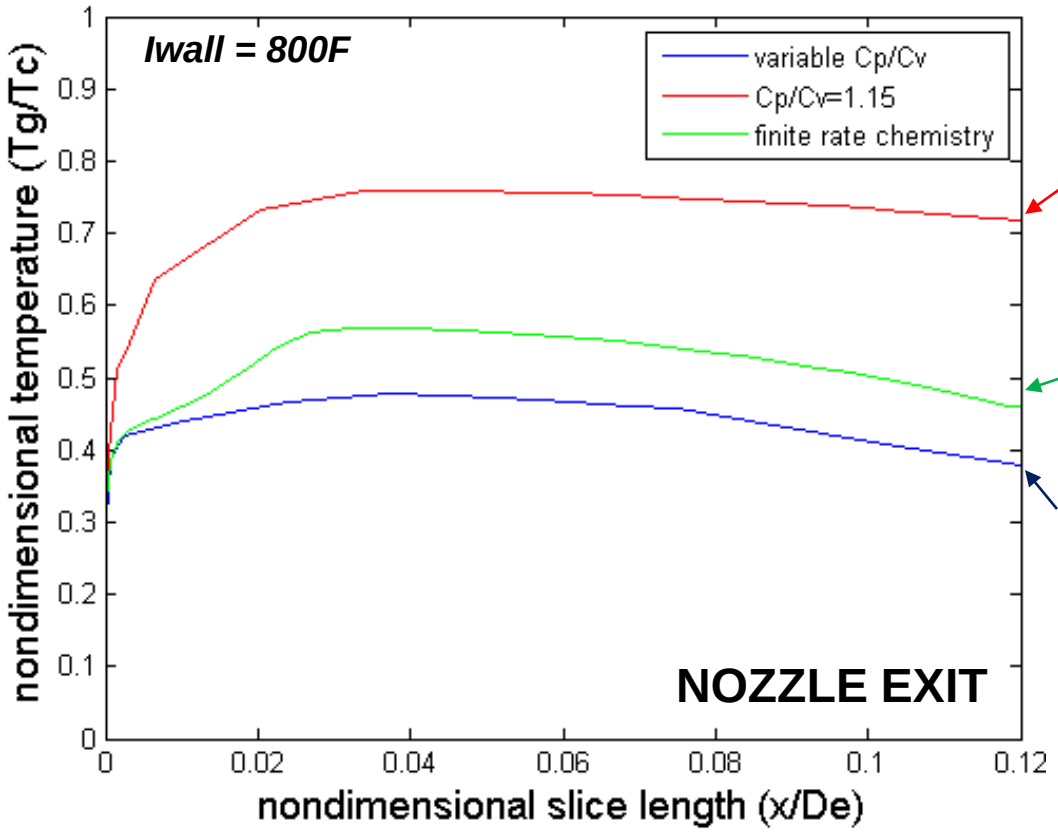

Model only accounts for translational and rotational molecular energy terms but frozen flow assumption

Model accounts for all (translational, rotational and vibrational) molecular energy terms and includes finite-rate chemistry

Model accounts for all molecular energy terms but frozen flow assumption

RAMP2 – Loci-CHEM Modeling Comparison

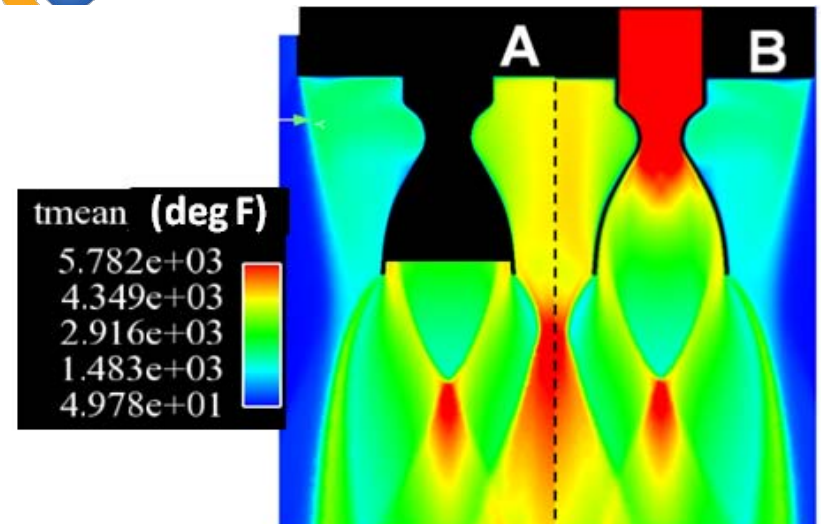

Minor deviation within thermal boundary layer profile (C) leads to minor differences in base heat flux and gas temperature distributions (D) and temperature contours (A and B).

Both modeling approaches provide similar base heating predictions

Loci-CHEM w/RAMP2-BLIMPJ Prescribed Boundary Condition

Loci-CHEM w/Finite Rate Nozzle Internal Flow Solution

Low Altitude

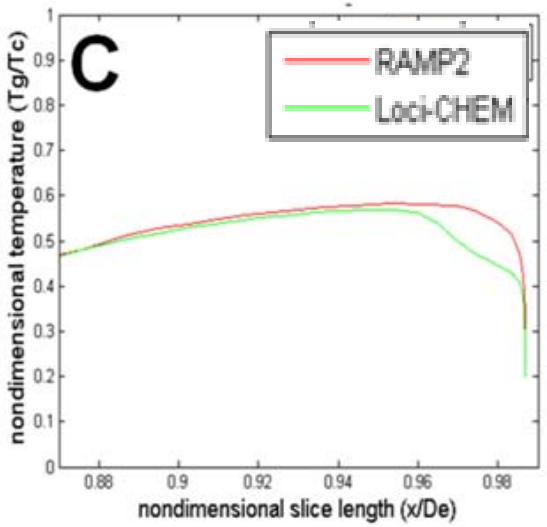

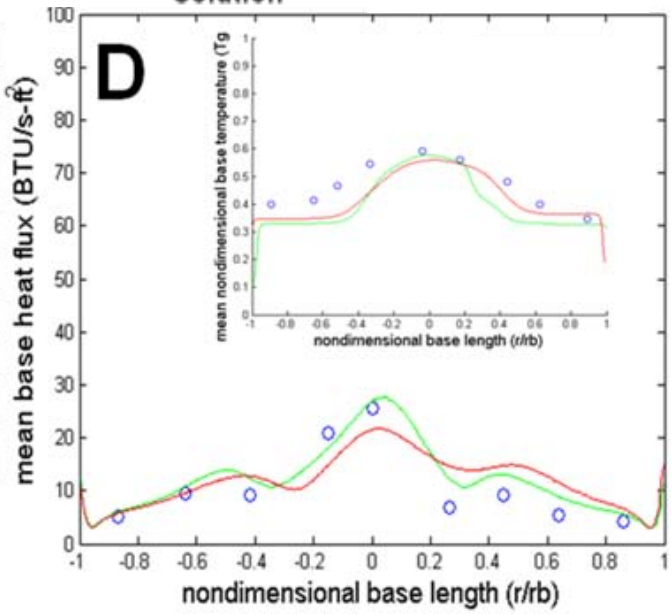

Boundary Layer Flow

Velocity vectors overlaid on static temperature contours show that the nozzle inner wall boundary layer rebounds off the Type I shock-shock induced pressure gradient and flows upstream toward the base plate

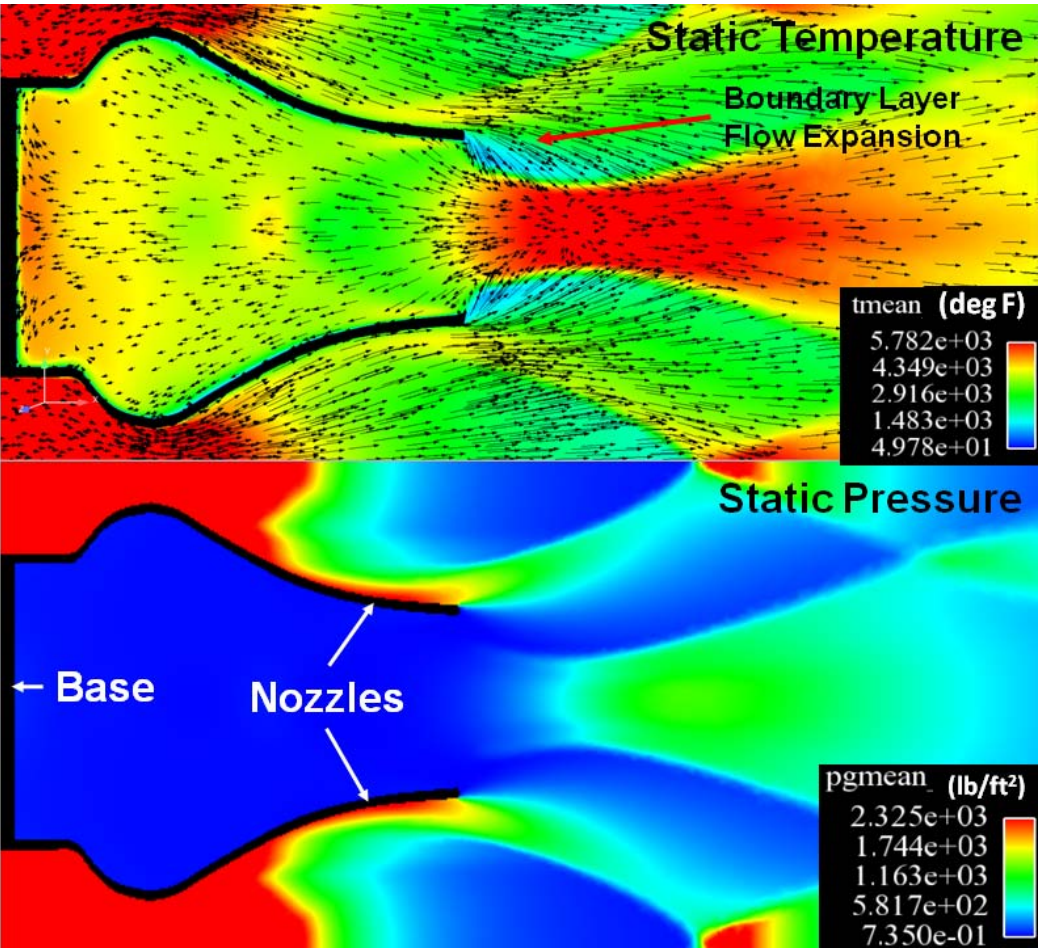

High Altitude

Cut plane through nozzle centerline

Recovery Shock & Recirculation Zone

Velocity vectors overlaid on Mach and pressure contours show the supersonic updraft plume develops an unstable recovery shock at the base center and low-pressure recirculation zones.

High Altitude

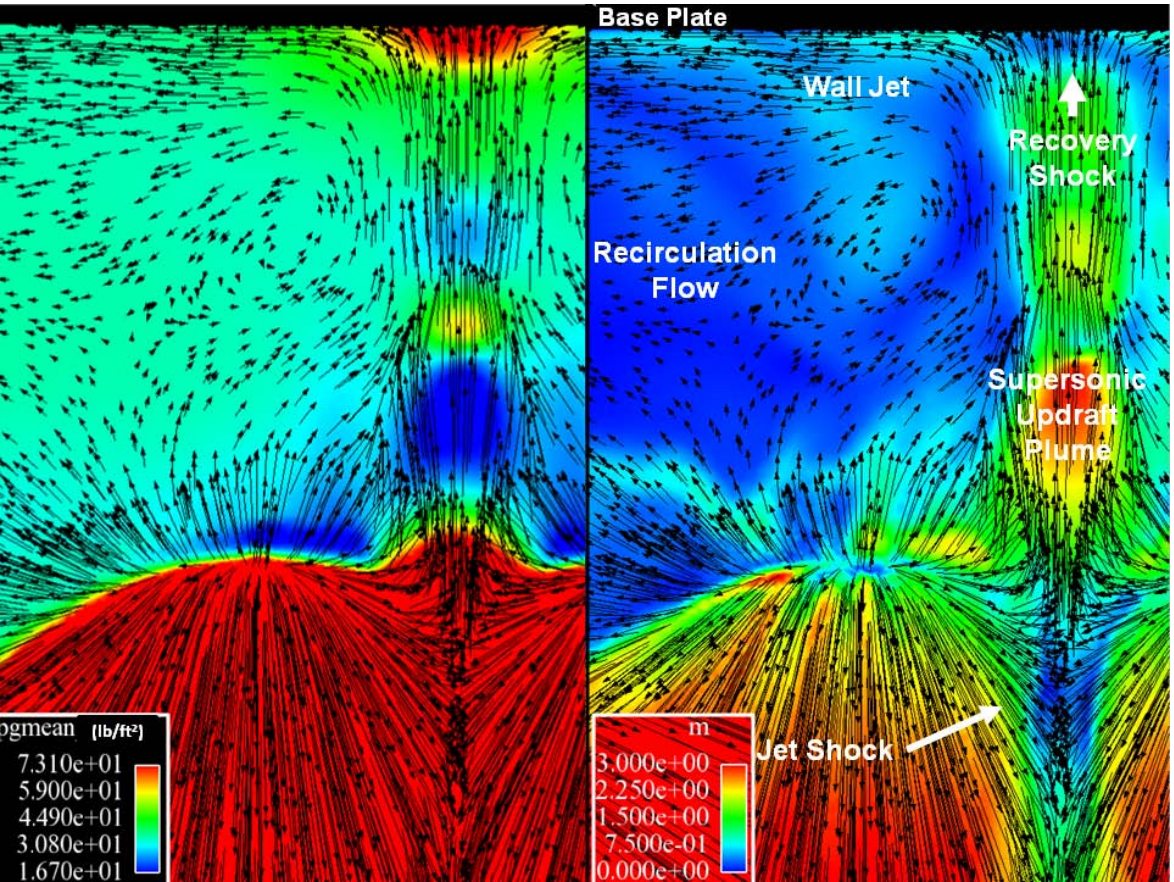

Leads to maximum peaks and perturbations in heat flux and pressure at the base plate center for high altitude case (momentum imbalance between the two structures). These responses are dampened by the denser freestream for the low altitude case.

Cut plane between two nozzles

Boundary Layer Chemical Reactions

Iwall boundary conditions (A) and shocks (B) change the plume chemical composition within the boundary layer – leads to a change in the thermal boundary layer profile and base heating characteristics

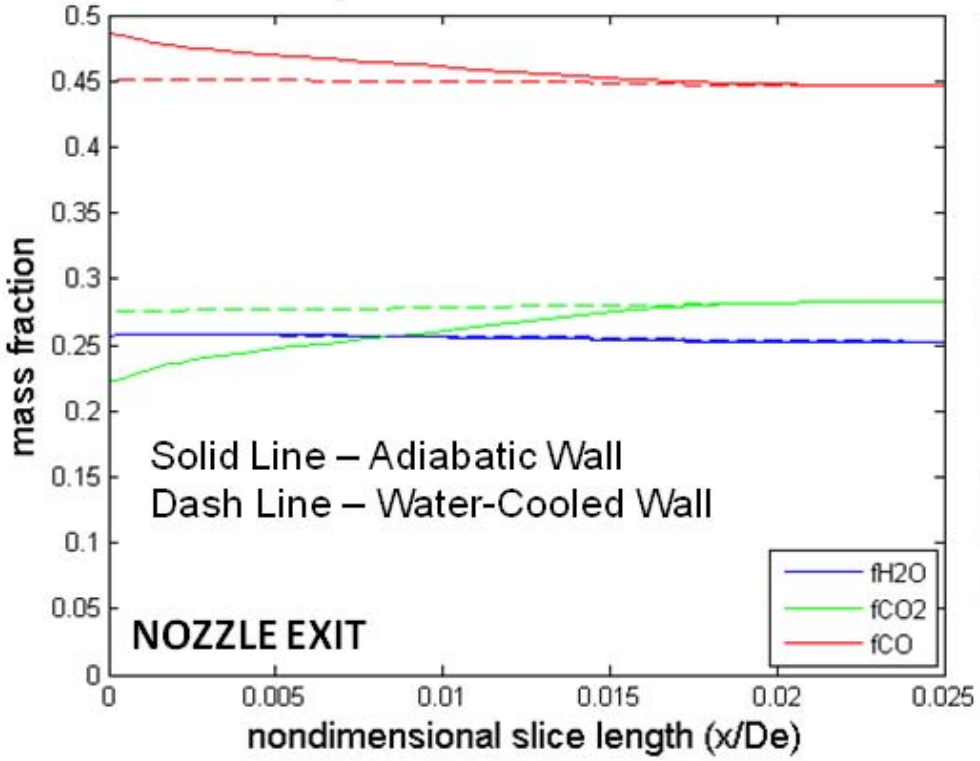

A

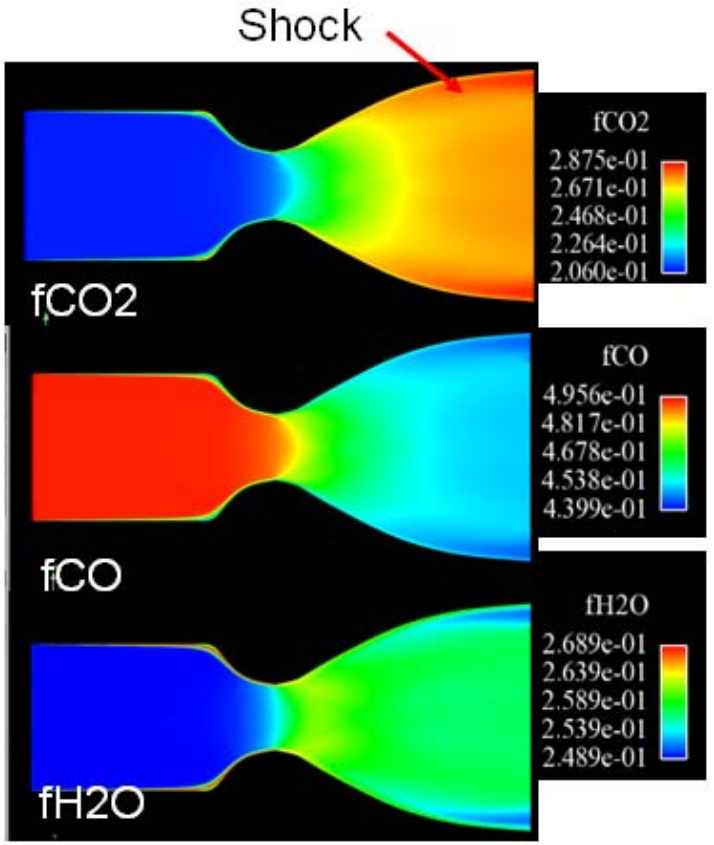

B

Afterburning

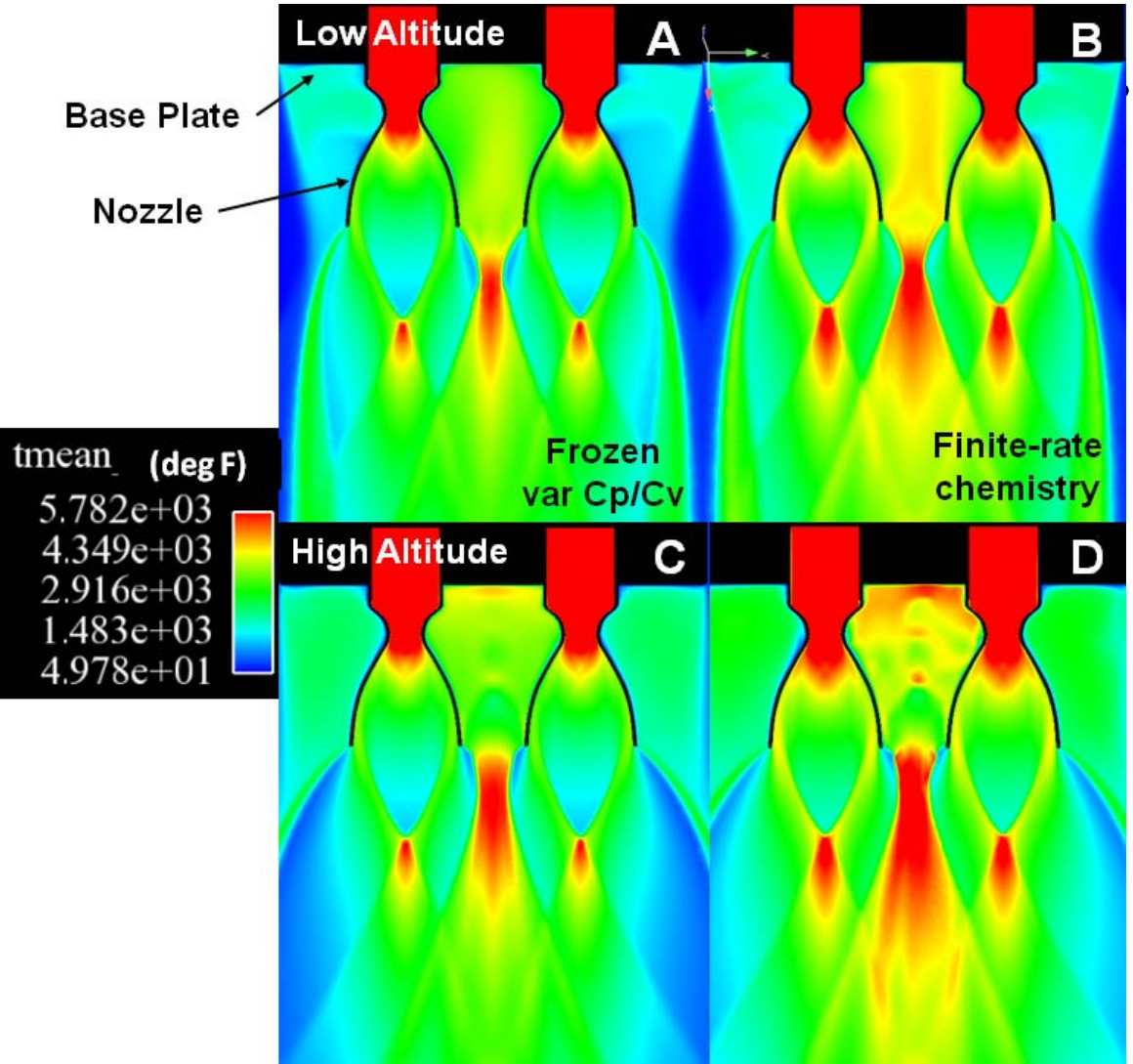

The mixing of the heavy carbon residual-exhaust species within the boundary layer and the ambient oxygen in the base region results in combustion and release of chemical energy within the updraft plume – leading to a rise in static temperature and base heat flux

Validation Study

Coleman and Stern Uncertainty Analyses

$$U_V^2 = U_D^2 + U_{SN}^2 + U_{SPD}^2$$ Validation Uncertainty

Data Uncertainty	Numerical Solution Uncertainty	Previous Data Uncertainty

$$E = D - S$$ Comparison Error

$$|E| \le U_V$$ Validation Criterion

Base heat flux solutions for the highest fidelity simulations are validated.

Validation of base pressure and base gas temperature solutions were also observed.

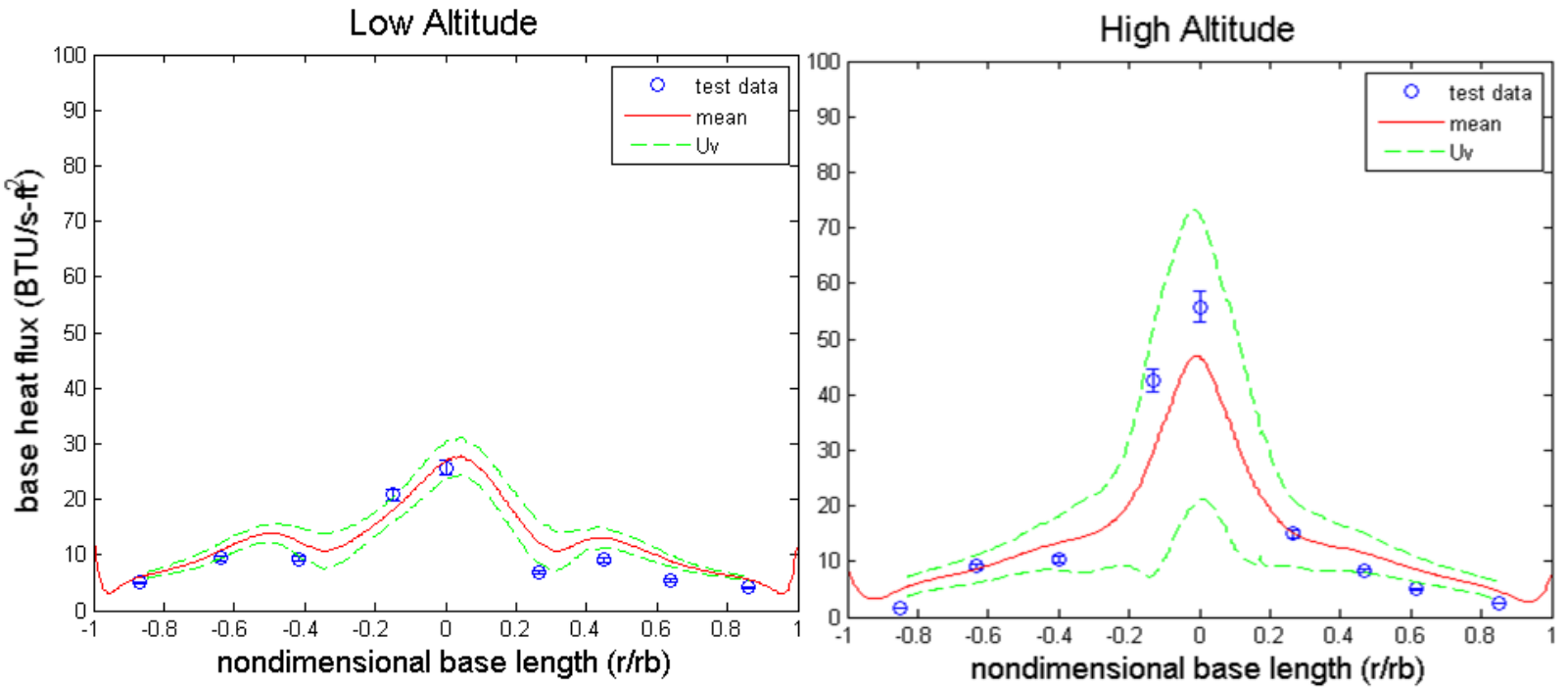

Conclusions

- Base heating characteristics are dependent on:
  - Nozzle inner wall thermal boundary layer
  - Recovery shock dynamics
  - Afterburning
- Thermal boundary layer is most sensitive to:
  - Iwall temperature
  - Thermodynamic models
  - Modeling of chemical reactions within boundary layer
- Base heating characteristics were not as sensitive to turbulence modeling or Twall conditions.
- Sensitivity study shows that well posed nozzle inner wall boundary conditions and accurate thermodynamics and finite-rate chemistry modeling with Loci-CHEM CFD can provide validated solutions.